

Changhui Liu

Mem. ASME

School of Mechanical Engineering,
Shanghai Jiao Tong University,
Shanghai 200240, China;
School of Mechanical Engineering,
Tongji University,
Shanghai 201804, China
e-mail: liuchanghui@sjtu.edu.cn

Tao Liu

School of Mechanical Engineering,
Shanghai Jiao Tong University,
Shanghai 200240, China
e-mail: jaymy@sjtu.edu.cn

Juan Du¹

School of Industrial and Systems Engineering,
Georgia Institute of Technology,
Atlanta, GA 30332
e-mail: juan.du@isye.gatech.edu

Yansong Zhang

School of Mechanical Engineering,
Shanghai Jiao Tong University,
Shanghai 200240, China
e-mail: zhangyansong@sjtu.edu.cn

Xinmin Lai

School of Mechanical Engineering,
Shanghai Jiao Tong University,
Shanghai 200240, China
e-mail: xmlai@sjtu.edu.cn

Jianjun Shi

Fellow ASME

School of Industrial and Systems Engineering,
Georgia Institute of Technology,
Atlanta, GA 30332
e-mail: jianjun.shi@isye.gatech.edu

Hybrid Nonlinear Variation Modeling of Compliant Metal Plate Assemblies Considering Welding Shrinkage and Angular Distortion

Ship assembly involves thousands of large dimensional compliant metal plates. These compliant metal plates are fully welded together by seam welding in the assembly process. Different from the automobile and aerospace assembly process, the final variation of ship assembly is significantly influenced by the geometric nonlinearity and welding deformation generated during the seam welding process. This paper develops a nonlinear variation model (NVM) to consider the geometric nonlinearity, welding shrinkage, and angular distortion based on elastic mechanics. Furthermore, the nonlinear variation model is calibrated by the composite Gaussian process (CGP) to compensate for other factors that are not considered in the nonlinear variation model. The proposed model is validated by a case study on the deviation prediction of an assembly of two compliant metal plates and compared with the existing methods. The results show that the proposed model has a significant improvement in prediction accuracy of assembly deviation.

[DOI: 10.1115/1.4046250]

Keywords: ship assembly, compliant metal plate assembly, welding deformation, geometric nonlinearity, dimensional deviation prediction, assembly, modeling and simulation, welding and joining

1 Introduction

The dimensional variation reduction and control of compliant metal plate assemblies play a key role in improving production efficiency and reducing the costs in the shipbuilding industry. A large ship hull is usually welded by thousands of large dimensional compliant metal plates, which is a typical multi-stage assembly process. The dimensional variation is critical to both quality and efficiency in the multi-stage ship hull assembly process. If there is a very small dimensional deviation from the designed shape at single-stage assembly, it can easily stack up to significant dimensional misalignments of large blocks (e.g., subassemblies) and makes it challenging to meet the assembly requirement of hull butt joint [1]. As a result, a large amount of dimensional trimming and surface treatments are needed, which is time-consuming, low efficiency, and high cost in ship assembly.

For the ship hull assembly process, it is common that the compliant ship parts are fully welded by seam welding, such as arc welding and laser welding, to prevent sea water from seeping into the hull. During the assembly process, some dimensional deformations exist

due to both the compliant (i.e., nonrigid) property of parts [2] and local welding. Because of the compliant property, the local welding deformation will significantly impact the global dimensional variation in the fixtured assembly process. In general, welding deformations are classified into shrinkage, angular distortion, bending, and buckling [3]. Among them, welding shrinkage and angular distortion have the most critical impacts on the final assembly variations [4]. However, current assembly variation modeling and analysis methodologies, such as the method of influence coefficients (MIC) [5], stream of variation (SoV) method [6], cannot effectively handle the deformation induced by local welding. Therefore, further study is urgently needed to consider welding shrinkage and angular distortion in variation modeling and analysis for the ship hull assembly process.

In general, the finite element method (FEM) is a powerful tool for accurate prediction of welding distortions [7,8]. In the past decades, researchers have studied intensively in improving the performance of FEM. Murakawa et al. [9] proposed an FEM for predicting distortions of structures under welding assembly based on inherent deformation and interface element. In the further study, the iterative substructure method was employed in the inherent strain method for large-scale welding parts [10]. By accounting for the highly nonlinear behavior and the transient phenomenon in the welding process, the thermal-elastic-plastic FEM can achieve high

¹Corresponding author.

Manuscript received September 7, 2019; final manuscript received January 29, 2020; published online February 5, 2020. Assoc. Editor: Wayne Cai.

prediction accuracy. Huang et al. [11] employ a local solid model and a global shell model for fast prediction of distortion in laser-welded thin sheets. In their study, a transient thermo-elastic-plastic analysis was used on the local three-dimensional solid model to obtain the inherent strain for the global shell model.

In the practical manufacturing process, some random part deviations induced in the former stage are unavoidable. In order to carry out the statistical variation analysis, the most direct and widely used method is the direct Monte Carlo simulation (MCS) [12–14], which combines statistical analysis and FEM. In order to consider both welding deformation and geometric tolerances on parts, Pahkamaa et al. [15] used MCS to generate a number of different non-nominal parts in CAD software, and these samples with deviations due to positioning error are exported to a welding simulation software. However, this method is time-consuming and needs intensive modeling and simulation efforts. This is especially true for the welding process due to its thermal-elasto-plastic characteristics that demand large computational costs in FEM simulation [16]. Lorin et al. [17] proposed a steady-state convex hull volumetric shrinkage (SCV) method to simplify the welding process simulation so that the efficiency of the combination analysis between geometric variation and welding distortion can be improved. However, this work focuses on rigid variation simulation only.

For a nonrigid variation simulation, the classical method is MIC [5]. In this method, the relationships between the part and assembly deviations are linked by a sensitivity matrix, which is obtained according to the constant linear force–displacement relationship. Thus, MIC establishes a linear and explicit variation propagation model for the compliant sheet metal assemblies. To further improve the accuracy of variation analysis, Yu et al. [18] derived the material variation-induced influence coefficients by MIC. Dahlström and Lindkvist [19] developed a contact model which considers the contact effect between parts to avoid penetrations based on MIC. Following this idea, Lupuleac et al. [20] formulated a quadratic programming problem to solve the contact problem in the MIC-based nonrigid variation simulation. By combining the theory of SoV modeling and analysis [6], MIC was further extended to multi-station assembly processes. Camelio et al. [21] developed a methodology for the dimensional variation propagation analysis in a multi-station compliant assembly system based on MIC and a state-space model, which considers the part variation, fixture variation, and welding gun variation. Furthermore, Yue et al. [22] defined three product-oriented indices to measure the variation influence of individual parts at a particular station to the dimensional quality of a final assembly. Zhang and Shi [23,24] extended the MIC model to the compliant composite part assembly by deriving the relationship between external assembly forces and the deformation of the composite part, which considers the anisotropic characteristics of composite materials. Söderberg et al. [25] employed the MCS/MIC simulation to find the stress distribution for a composite part assembly.

These MIC-based studies have been widely applied in variation modeling and analysis of the assembly process of the automobile body [26–28] and aircraft fuselage or wing [29–31]. These assembly processes mainly focus on spot welding or riveting to assemble two parts together, so the local deformation (such as hot deformation near spot welding and plastic deformation near riveting point) can be neglected. At the same time, the stiffness matrix in these assembly processes can be treated as a constant due to the small assembly variation, which is one of the main assumptions of MIC. Such an assumption is valid only when the assembly variation is much smaller than the source of variations (e.g., part manufacturing error and fixture error [32,33]) because the stiffness matrix of the assembly actually varies with the geometrical variation [34,35].

In order to prevent seawater from seeping into the hull, the compliant plates of the hull have to be fully welded by seam welding. Compared with other types of assembly processes such as spot welding and riveting, the deformation induced by seam welding is much larger and has a great impact on the assembly variation

[36]. On one hand, the seam welding distortion, especially the angular distortion, will result in large assembly variation compared with other source of variations. On the other hand, the seam welding shrinkage in the plane will bring the axial or in-plane loads in the spring-back step for the fixtured assembly [37]. All of these mechanical behaviors will significantly change the out-of-plane stiffness that leads to spring back with unneglectable nonlinear behaviors. Therefore, the stiffness matrices obtained from the constant linear relationship is no longer valid. For the same reason, the existing MIC-based compliant variation model cannot be applied to the compliant metal plate assemblies for the ship hull manufacturing.

In this paper, we proposed a hybrid nonlinear variation model (HNVM) for the compliant metal plate assembly, which includes the nonlinear variation modeling and model calibration. Compared with the current literature, the nonlinear variation model (NVM) considers the geometric nonlinear mechanical behavior occurred in the spring back, and the welding shrinkage and angular distortion generated in the seam welding. The dimensional deviations induced by other factors are considered by calibration of the NVM to further improve the accuracy of the proposed model.

The remainder of this paper is organized as follows: Sec. 2 develops a HNVM for the compliant metal plate assembly in the ship hull manufacturing. In Sec. 3, a case study is conducted to validate the proposed model. Section 4 discusses the conclusions, limitations, and some future works.

2 Hybrid Nonlinear Variation Modeling

This section presents the detail derivations for the proposed hybrid nonlinear variation model. Section 2.1 introduces the NVM without considerations of welding shrinkage and angular distortion. In Sec. 2.2, the impacts of welding shrinkage and angular distortion are modeled and integrated to the NVM in Sec. 2.1. To further improve the NVM accuracy, Sec. 2.3 conducts model calibration to capture other welding deformation effects that are not considered in the NVM. In this paper, we name the NVM after the calibration as the HNVM.

An overview of the proposed method is shown in Fig. 1. According to the geometric and material parameters, the NVM is established based on the nonlinear elastic mechanics first, which parameterizes the welding shrinkage and angular distortion. Then the welding shrinkage and angular distortion computed by the

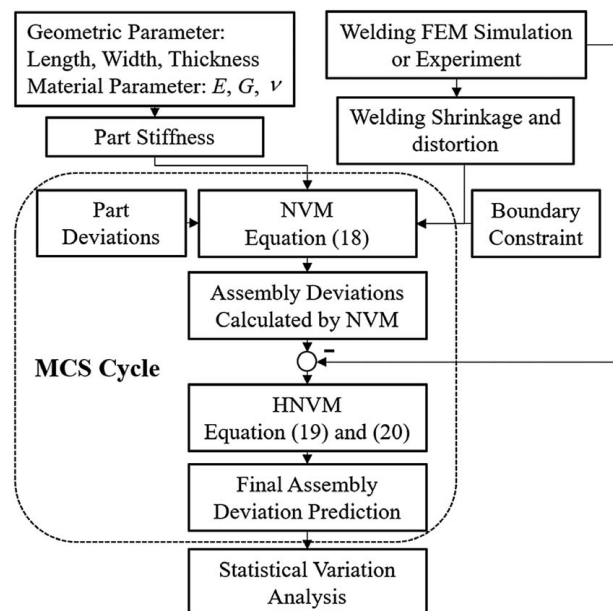


Fig. 1 Flowchart of the proposed method

welding FEM simulation software are integrated into the NVM. Thus, the assembly deviation can be directly calculated according to the part deviation quickly. In order to improve the prediction accuracy, the prediction error with respect to the welding FEM simulation is calculated to calibrate the NVM. Finally, we predict the final assembly deviation for the compliant metal plate assembly considering welding shrinkage and angular distortion with high precision using the proposed HNVM. The statistical assembly variation analysis can be implemented by generating different part deviations and the repeated welding FEM simulations are avoided in the proposed method.

2.1 Variation Model Considering Geometric Nonlinearity.

In Sec. 2.1.1, the main steps and the corresponding mechanism for the compliant plate assembly are introduced to illustrate the geometric nonlinearity in the ship assembly. After that, Sec. 2.1.2 develops the variation model considering geometric nonlinearity. It should be noted that Sec. 2.1 focuses on the global representation of the variation model which is based on the element formulation. More detail discussions about the element representation will be provided in Sec. 2.2.1.

Before discussing the details of the modeling results, we have the following basic assumptions: (i) the deformation caused by gravity is not considered in the modeling. (ii) Only dimensional variations in the normal direction (i.e., direction along the thickness) of parts are considered. (iii) The proposed nonlinear model is based on the nonlinear elastic mechanics and the material of parts is assumed to be homogeneous and isotropic. (iv) The material parameters are independent on the temperature in the proposed nonlinear model.

Here are some discussions about the justifications of the assumptions above. In terms of assumption (i), it is similar to Refs. [32,33]

for variation modeling of the ship plates' assembly. The hull block is a kind of box structure [1], which consists of two main categories of plates. One category is that the normal direction of the plate is perpendicular to the direction of gravity, such as girder, solid floor. For these plates, the gravity has no impact on the assembly deviation in the normal direction. Another category is that the normal direction of the plate is parallel to the direction of gravity, such as the bottom plate, deck. Though the sizes of these plates are big, they are welded by a lot of girders and solid floors in the gravity direction. For these plates, the deviations caused by gravity are very small. In terms of assumption (ii), the ratio of the part thickness to the length or the width is very small (3:1000 ~ 12:1000) in the shipbuilding industry. Thus, the in-plane welding shrinkage relative to the length and the width of parts is very small. In addition, the in-plane dimensional variations are restricted in the fixtured assembly process in our study. Assumptions (iii) & (iv) are the base of proposed elastic NVM, which means that the heat transfer process, plastic deformation process, and phase transformation process are not considered in NVM. However, their influences on the final assembly deviation are compensated in the model calibration, which will be discussed in Sec. 2.3.

2.1.1 Analysis of a Compliant Assembly. The variation model for assembly of compliant plates will consider all mechanic interactions involved in a single station, including positioning, clamping, welding, and releasing (i.e., PCWR, as shown in Fig. 2). More discussions on each of those mechanical actions are provided as follows:

- (1) **Positioning** (Fig. 2(a)): In order to develop the variation model, a right-hand coordinate system is used. The origin of the coordinate system is defined at the joint point of two

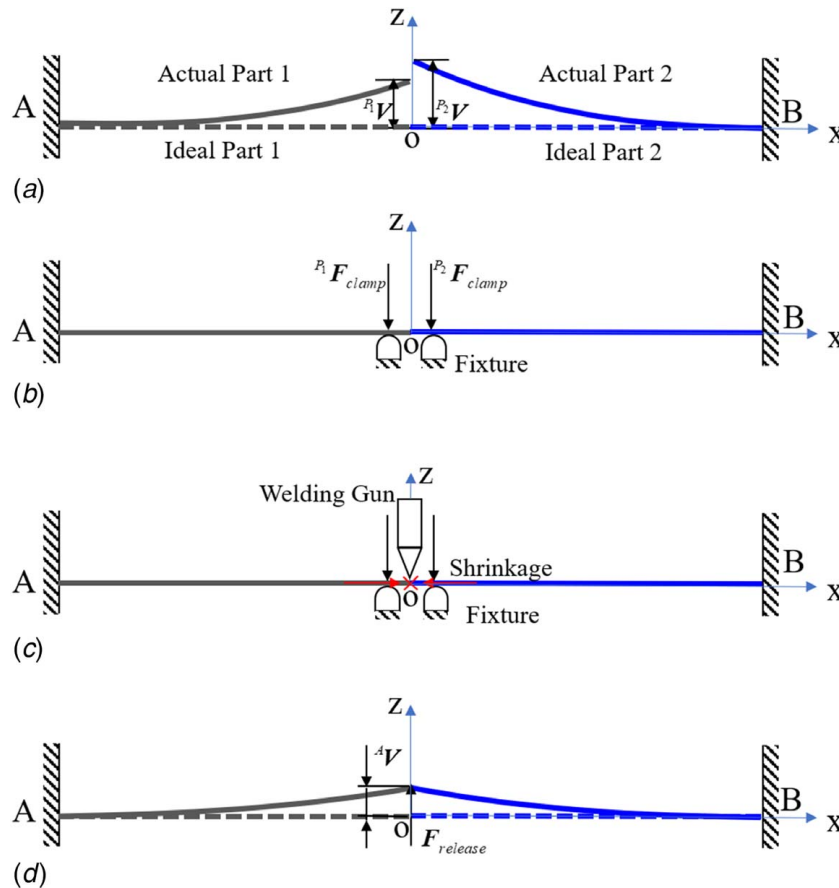


Fig. 2 PCWR cycle: (a) positioning, (b) clamping, (c) welding, and (d) releasing (figure revised from Ref. [23])

ideal parts. It is also the starting point of seam welding. The x axis is along the AB direction as shown in Fig. 2(a). In the positioning process, the fixed plate is assumed to be a cantilever plate, with one end of these two plates (end A and end B) positioned to the locating fixtures. The deviations in the z -direction of the assembled pair of plates caused by manufacturing errors are denoted by vectors ${}^P_1\mathbf{V}$ and ${}^P_2\mathbf{V}$ if each plate has more than one source of variation. Then, the deviation of these two parts is illustrated as

$${}^P\mathbf{V} = \begin{Bmatrix} {}^P_1\mathbf{V} \\ {}^P_2\mathbf{V} \end{Bmatrix} \quad (1)$$

- (2) *Clamping* (Fig. 2(b)): The parts with dimensional deviations are clamped to their nominal positions by applying a set of clamping forces at certain clamping points. In this step, a fundamental assumption is that a linear relationship exists between the clamping forces and deflections because the deviations of the parts are very small with respect to the size of the parts; and there is no in-plane force generated. If we use vector \mathbf{F}_{clamp} to denote the total clamping force and \mathbf{K}_{clamp} to denote the stiffness matrix in the clamping step, then the constant linear force–displacement relationship can be represented as

$$\mathbf{F}_{clamp} = -\mathbf{K}_{clamp} \cdot {}^P\mathbf{V} \quad (2)$$

- (3) *Welding* (Fig. 2(c)): In a ship assembly process, a seam welding is used to assemble the two plates together while the clamping forces are still applied to hold both plates. If end A and end B are not fixed in the x -direction, the dimensional shrinkage in the x -direction will be generated and make the width of the assembled plates smaller than that before welding. However, end A and end B are fixed in the welding assembly process. Although the dimensional shrinkage in the x -direction is restricted, the shrinkage in the z -direction is still generated along the weld seam due to the material solidification, which will bring the axial loads in the x -direction and increase the out-of-plane stiffness of the assembly.

- (4) *Releasing* (Fig. 2(d)): After welding, the spring back of the assembly occurs when the clamping forces are released. The spring-back deviations are determined by the releasing force $\mathbf{F}_{release}$ and stiffness matrix of the assembly. The releasing force $\mathbf{F}_{release}$ is assumed to have the same magnitude as the clamping forces \mathbf{F}_{clamp} [5,32,33]. However, the stiffness matrix of the assembly is quite different from that before welding. Due to the influence of welding distortion and in-plane loads induced by in-plane shrinkage, the stiffness matrix of the assembly will increase and vary with the spring-back deviations. Thus, the constant linear force–displacement relationship does not hold in such a case. In order to improve the accuracy of variation analysis, a nonlinear relationship between the releasing force $\mathbf{F}_{release}$ and the assembly deviation ${}^A\mathbf{V}$ is represented as

$$\mathbf{K}_S({}^A\mathbf{V}) \cdot {}^A\mathbf{V} = \mathbf{F}_{release} \quad (3)$$

where the secant stiffness $\mathbf{K}_S({}^A\mathbf{V})$ is dependent on the assembly deviation ${}^A\mathbf{V}$. The expression of $\mathbf{K}_S({}^A\mathbf{V})$ consists of different order terms of ${}^A\mathbf{V}$. In this paper, only two orders are considered, then $\mathbf{K}_S({}^A\mathbf{V})$ can be expressed as the following formula:

$$\mathbf{K}_S({}^A\mathbf{V}) = \mathbf{K}_L + \mathbf{K}_{N1}({}^A\mathbf{V}) + \mathbf{K}_{N2}({}^A\mathbf{V}) \quad (4)$$

where \mathbf{K}_L is a constant stiffness matrix which is the linear term (represented by L). $\mathbf{K}_{N1}({}^A\mathbf{V})$ and $\mathbf{K}_{N2}({}^A\mathbf{V})$ denote the first-order nonlinear (represented by $N1$) term and the second-order nonlinear (represented by $N2$) term, respectively. By considering Eq. (3), Eq. (4) can be further

represented as:

$$(\mathbf{K}_L + \mathbf{K}_{N1}({}^A\mathbf{V}) + \mathbf{K}_{N2}({}^A\mathbf{V})) \cdot {}^A\mathbf{V} = \mathbf{F}_{release} \quad (5)$$

Equation (5) shows that the relationship between the releasing force $\mathbf{F}_{release}$ and the assembly deviation ${}^A\mathbf{V}$ is complicated, and the releasing force can be divided into a linear term and two nonlinear terms.

2.1.2 Variation Modeling. The releasing force $\mathbf{F}_{release}$ has the same magnitude as the clamping force \mathbf{F}_{clamp} , but opposite in the direction [5,32,33], i.e.

$$\mathbf{F}_{release} = -\mathbf{F}_{clamp} \quad (6)$$

Considering Eq. (2), the mechanical equilibrium Eq. (5) in the releasing process can be rewritten as

$$(\mathbf{K}_L + \mathbf{K}_{N1}({}^A\mathbf{V}) + \mathbf{K}_{N2}({}^A\mathbf{V})) \cdot {}^A\mathbf{V} = \mathbf{K}_{clamp} \cdot {}^P\mathbf{V} \quad (7)$$

Equation (7) establishes the nonlinear relationship between part deviation and assembly deviation. Notably, if we only consider the constant stiffness matrix \mathbf{K}_L , Eq. (7) is degenerated into the equilibrium equation in MIC.

In this study, the geometric nonlinear mechanical behavior is considered in the variation model. Since the secant stiffness matrix $\mathbf{K}_S({}^A\mathbf{V})$ is dependent on ${}^A\mathbf{V}$, the inverse of the secant stiffness matrix $\mathbf{K}_S({}^A\mathbf{V})$ cannot be obtained directly. In order to solve the Eq. (8), we rewrite Eq. (7) as

$$\boldsymbol{\psi}({}^A\mathbf{V}) = \mathbf{K}_S({}^A\mathbf{V}) \cdot {}^A\mathbf{V} - \mathbf{K}_{clamp} \cdot {}^P\mathbf{V} = \mathbf{0} \quad (8)$$

To account for the axial or in-plane loads, the secant stiffness matrix $\mathbf{K}_S({}^A\mathbf{V})$ of the assembly must be recalculated from the deformed geometry. In this paper, *Newton–Raphson* method is applied to account for the incremental updates of the stiffness matrix. If only the first order of the increment deviation, i.e., $\Delta^A\mathbf{V}$, is considered, the nonlinear equation can be written as

$$\begin{aligned} \boldsymbol{\psi}({}^A\mathbf{V}^{n+1}) &= \boldsymbol{\psi}({}^A\mathbf{V}^n + \Delta^A\mathbf{V}^n) = \boldsymbol{\psi}({}^A\mathbf{V}^n) \\ &+ \left(\frac{\partial \boldsymbol{\psi}}{\partial {}^A\mathbf{V}} \right)_{{}^A\mathbf{V}={}^A\mathbf{V}^n} \cdot \Delta^A\mathbf{V}^n = \mathbf{0} \end{aligned} \quad (9)$$

($n = 0, 1, 2, \dots$)

where n denotes the number of iterations and $\left(\frac{\partial \boldsymbol{\psi}}{\partial {}^A\mathbf{V}} \right)$ is a Jacobi Matrix. Then, we get the first order of the increment deviation

$$\Delta^A\mathbf{V}^n = -(\mathbf{K}_T^n)^{-1} \cdot \boldsymbol{\psi}({}^A\mathbf{V}^n) \quad (10)$$

where $\mathbf{K}_T^n = \mathbf{K}_T({}^A\mathbf{V}^n) = \left(\frac{\partial \boldsymbol{\psi}}{\partial {}^A\mathbf{V}} \right)_{{}^A\mathbf{V}={}^A\mathbf{V}^n}$ is the secant stiffness matrix at the n th iteration.

Because ${}^A\mathbf{V}^{n+1} = {}^A\mathbf{V}^n + \Delta^A\mathbf{V}^n$, the $(n+1)$ th approximation for the assembly deviation can be expressed as

$${}^A\mathbf{V}^{n+1} = {}^A\mathbf{V}^n + (\mathbf{K}_T^n)^{-1} \cdot [\mathbf{K}_{clamp} \cdot {}^P\mathbf{V} - \mathbf{K}_S^n \cdot {}^A\mathbf{V}^n] \quad (11)$$

where $\mathbf{K}_S^n = \mathbf{K}_S({}^A\mathbf{V}^n)$ is the tangent stiffness matrix at the n th iteration.

Equation (11) gives an approximate solution for Eq. (7). The iterative procedure is illustrated in Fig. 3. The nonlinear relationship between the releasing force $\mathbf{F}_{release}$ and the assembly deviation ${}^A\mathbf{V}$ is represented by the curve. \mathbf{K}_T^n is the tangent slope of the point $({}^A\mathbf{V}^n, \mathbf{F}_{release}({}^A\mathbf{V}^n))$. The solution of the final assembly deviation ${}^A\mathbf{V}^*$ is to meet the condition $\mathbf{F}_{release}({}^A\mathbf{V}^*) = -\mathbf{F}_{clamp}$. To better illustrate this condition, point B corresponds to the final solution of ${}^A\mathbf{V}^*$ in Fig. 3.

The iteration will not end until $\|\Delta^A\mathbf{V}^n\|_2 \leq \xi$, where ξ is the convergence threshold. It can be shown that if $n=0$ and ${}^A\mathbf{V}^0 = \mathbf{0}$, the nonlinear model illustrated by Eq. (11) is degenerated into the linear

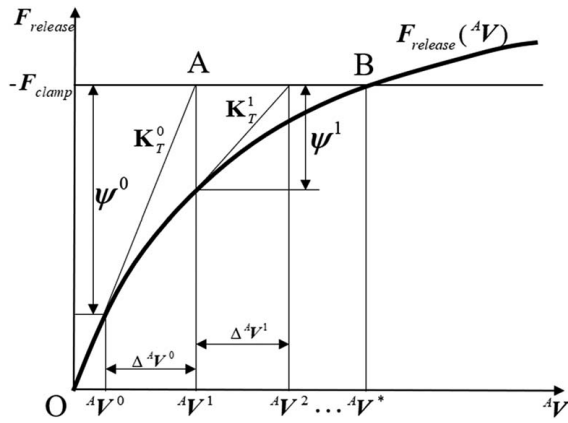


Fig. 3 The iterative procedure for obtaining the final assembly deviation ${}^A V^*$

MIC model, thereby indicating that the MIC model is a simplified form of nonlinear model under linear condition.

2.2 Nonlinear Variation Model Considering Welding Shrinkage and Angular Distortion. In this section, the NVM is first represented by finite element form to consider the interaction between degrees-of-freedom (DOFs) in Sec. 2.2.1. Then, the welding constraint is proposed to consider welding shrinkage and angular distortion in Sec. 2.2.2. Finally, in Sec. 2.2.3, we propose the global constraint equation and develop an element representation for the NVM considering welding shrinkage and angular distortion.

2.2.1 Element Representation. In order to account for the influence of welding shrinkage and angular distortion, the interaction between DOFs in different directions cannot be ignored. Without loss of generality, a common rectangular plate shell element is used in this paper. The generalized displacements $(u_0, v_0, w_0, \phi_x, \phi_y)^T$ in the first-order plate theory (Mindlin theory) [38] are applied, which considers five DOFs of a point in a plate. In this theory, $u_0, v_0,$ and w_0 denote the deformation of a point at the referential mid-plane in $x-, y-,$ and $z-$ directions, respectively. ϕ_x and ϕ_y denote the rotation angles of the normal to the cross section with respect to the $y-$ and the $x-$ axes caused by in-plane deformation. Correspondingly, the equilibrium equation for any element nodal can be formulated by

$${}^e \mathbf{K}_S({}^e \mathbf{V}) \cdot {}^e \mathbf{V} = {}^e \mathbf{F} \quad (12)$$

where ${}^e \mathbf{V}, {}^e \mathbf{F},$ and ${}^e \mathbf{K}_S({}^e \mathbf{V})$ are the element displacement vector, the element external force vector, and the element nonlinear secant stiffness matrix, respectively. The detailed derivation of ${}^e \mathbf{K}_S({}^e \mathbf{V})$ is listed in the Appendix. The element nonlinear secant and tangent stiffness matrices, i.e., ${}^e \mathbf{K}_S({}^e \mathbf{V})$ and ${}^e \mathbf{K}_T({}^e \mathbf{V})$, can also be represented by Eqs. (13) and (14) [34]

$${}^e \mathbf{K}_S({}^e \mathbf{V}) = {}^e \mathbf{K}_L + {}^e \mathbf{K}_{N1}({}^e \mathbf{V}) + {}^e \mathbf{K}_{N2}({}^e \mathbf{V}) \quad (13)$$

$${}^e \mathbf{K}_T({}^e \mathbf{V}) = {}^e \mathbf{K}_L + 2{}^e \mathbf{K}_{N1}({}^e \mathbf{V}) + 3{}^e \mathbf{K}_{N2}({}^e \mathbf{V}) \quad (14)$$

where the linear item ${}^e \mathbf{K}_L$ is independent of ${}^e \mathbf{V}$, while the first-order and second-order nonlinear items, i.e., ${}^e \mathbf{K}_{N1}({}^e \mathbf{V})$ and ${}^e \mathbf{K}_{N2}({}^e \mathbf{V})$, are dependent on ${}^e \mathbf{V}$.

By assembling all the individual element stiffness matrices together, the global stiffness matrix can be constructed. Given the global stiffness matrix, all the nodal displacements of the assembly can be calculated by solving Eq. (11).

2.2.2 Welding Constraint. In order to consider the welding constraints, paired nodes of two assembled parts need to be

defined first. As shown in Fig. 4(a), the paired nodes are the nodes along the end of each plate. In the spot welding or riveting process, the paired nodes can be regarded as rigidly assembled together because the local deformation due to spot welding or riveting can be neglected. However, for the seam welding, the influence of the local welding deformation cannot be neglected. This is because after the seam welding, material shrinkage exists along the weld seam, thereby leading to a displacement for all nodes of the assembly except the nodes clamped by the fixtures at the end. As shown in Figs. 4(b) and 4(c), the vertical dash and solid lines denote the positions of the nodes before and after welding. In order to consider the deformation induced by the local welding, we propose the following welding constraint:

$${}^e \mathbf{V}_{i+1} - {}^e \mathbf{V}_i = {}^e \Delta \mathbf{i} \quad (15)$$

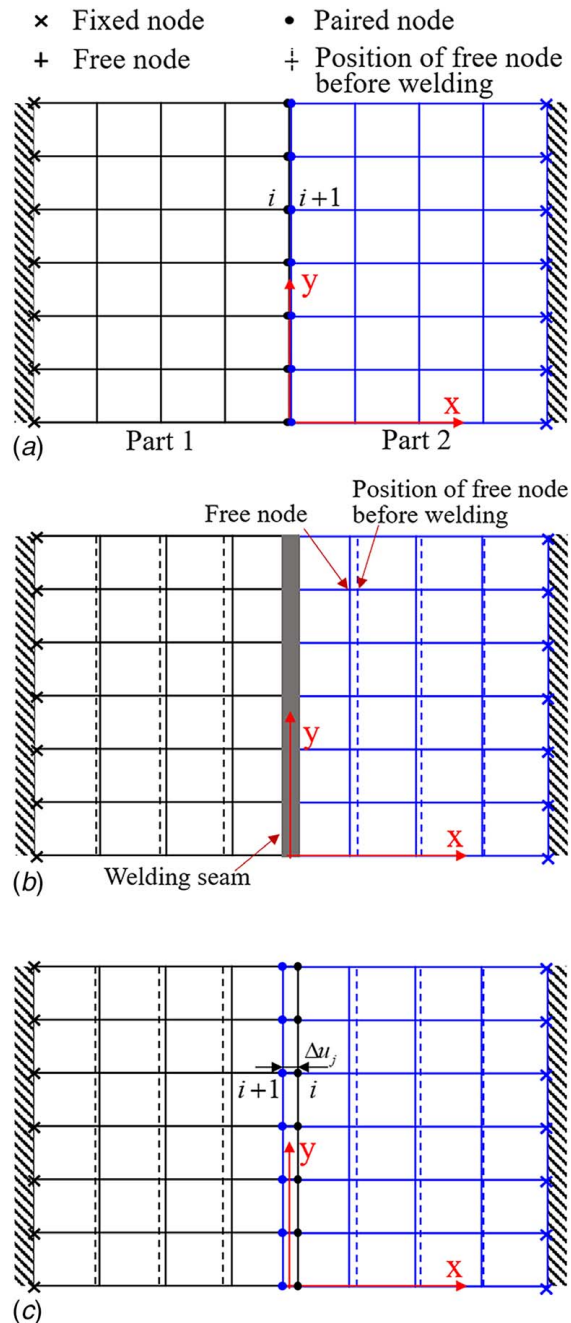


Fig. 4 Illustrations of nodal displacements: (a) before welding, (b) after welding, and (c) equivalent expression

where ${}^e\mathbf{d}_i = (\Delta u_i, \Delta v_i, \Delta w_i, \Delta \varphi_{x_i}, \Delta \varphi_{y_i})^T$ represents the relative displacement for the paired nodes $i + 1$ and i induced by the local welding deformation. Δu_i denotes the relative displacement in the x -direction, which is illustrated in Fig. 4(c). Similarly, Δv_i and Δw_i are the relative displacements in the y and z directions. $\Delta \varphi_{x_i}$ and $\Delta \varphi_{y_i}$ are angular distortions around the y - and x -axes, respectively.

2.2.3 Global Constraint Equation. Other than paired nodes along the weld seam, the fixed nodes should also satisfy the constraint that the DOFs of these nodes are zero (i.e., fixed constraint). In this paper, we assume that there are M nodes for the assembly, thereby indicating there are $5M$ DOFs. Among these DOFs, there are m DOFs must satisfy certain constraint condition such as welding constraint and fixed constraint. Then, the global constraint equation can be represented as

$$\mathbf{G} \cdot {}^A\mathbf{V} = \mathbf{d} \quad (16)$$

where ${}^A\mathbf{V} = (u_{01}, v_{01}, w_{01}, \varphi_{x1}, \varphi_{y1}, u_{02}, v_{02}, w_{02}, \varphi_{x2}, \varphi_{y2}, \dots, u_{0M}, v_{0M}, w_{0M}, \varphi_{xM}, \varphi_{yM})^T$ is the displacement vector of all nodes for the assembly. $\mathbf{d} = (d_1, d_2, \dots, d_m)^T$ is the displacement constraint vector. \mathbf{G} is a $m \times 5M$ coefficient matrix for the constraint equation.

According to the *Lagrangian multiplier* method [39], Eqs. (3) and (16) can be further written as

$$\begin{bmatrix} \mathbf{K}_S & \mathbf{G}^T \\ \mathbf{G} & \mathbf{0} \end{bmatrix} \cdot \begin{Bmatrix} {}^A\mathbf{V} \\ \lambda \end{Bmatrix} = \begin{Bmatrix} \mathbf{F}_{release} \\ \mathbf{d} \end{Bmatrix} \quad (17)$$

where $\lambda = (\lambda_1, \lambda_2, \dots, \lambda_m)^T$ is the *Lagrange multiplier*. Substitute Eqs. (11)–(17), we have

$$\begin{aligned} \begin{Bmatrix} {}^A\mathbf{V} \\ \lambda \end{Bmatrix}^{n+1} &= \begin{Bmatrix} {}^A\mathbf{V} \\ \lambda \end{Bmatrix}^n + \begin{bmatrix} \mathbf{K}_T^n & \mathbf{G}^T \\ \mathbf{G} & \mathbf{0} \end{bmatrix}^{-1} \cdot \left[\begin{bmatrix} \mathbf{K}_{clamp} & \mathbf{0} \\ \mathbf{0} & \mathbf{I} \end{bmatrix} \cdot \begin{Bmatrix} {}^P\mathbf{V} \\ \mathbf{d} \end{Bmatrix} \right. \\ &\quad \left. - \begin{bmatrix} \mathbf{K}_S^n & \mathbf{G}^T \\ \mathbf{G} & \mathbf{0} \end{bmatrix} \cdot \begin{Bmatrix} {}^A\mathbf{V} \\ \lambda \end{Bmatrix}^n \right] \end{aligned} \quad (18)$$

Equation (18) is the proposed NVM, which considers the welding shrinkage and angular distortion.

2.3 Nonlinear Variation Model With Calibration. As shown in the model assumption that NVM is based on elastic mechanics, the impact introduced by heat transfer process, plastic deformation process, and phase transformation process is not considered during the mechanical derivation. Thus, there may also exist some model errors near the weld seam. To improve NVM accuracy, this subsection will calibrate the NVM and propose the HNVM.

In general, the model calibration for each node can be formulated as

$${}^C V = w_0 + \delta \quad (19)$$

where ${}^C V$ is the deviation in the z -direction after calibration, and w_0 is a nodal displacement in the z -direction that is calculated by NVM (i.e., Eq. (18)) in Sec. 2.3. δ is the model deviation induced by other factors (such as plastic deformation, phase transformation, etc.) that are not considered in the NVM. However, such model deviation can be modeled as Gaussian process (GP) in general, which is a function of the locations on the plate, i.e., the coordinate locations of the node in x, y .

In the literature, GP model is widely used for approximating the computer experiments. Based on the GP model, composite Gaussian process (CGP) model is developed to approximate complex surfaces more accurately, which considers both global and local variations by a composite of two Gaussian processes [40]. The deviation prediction errors of nodes from NVM will be larger near the weld seam but smaller near the fixed end. Since a single Gaussian process can only capture the global variations

and cannot capture the local variations well, we use CGP to calibrate the nonlinear variation model. Thus, δ can be formalized as

$$\delta = f_{global}(x, y) + \sigma(x, y)f_{local}(x, y) \quad (20)$$

$$f_{global}(x, y) \sim GP(\mu, \tau^2 g(x, y)) \quad (21)$$

$$f_{local}(x, y) \sim GP(0, l(x, y)) \quad (22)$$

where (x, y) is the coordinate locations of all nodes in x, y . Figure 4 illustrates the coordinate of two assembled parts. The GP for global variations follows a distribution with the constant mean μ and variance τ^2 , and the correlation structure $g(x, y)$ requires smoothness to capture the global variations. $l(x, y)$ is a local correlation structure for modeling local variations. Overall, the CGP model for δ is equivalent to assuming $\delta \sim GP(\mu, \tau^2 g(x, y) + \sigma^2(x, y)l(x, y))$. $\sigma^2(x, y)$ can be further written as $\sigma^2(x, y) = \sigma^2 \theta(x, y)$, where $\theta(x, y)$ is the standardized volatility function fluctuating around the unit value; σ^2 is the constant variance. The equivalent CGP model indicates that δ follows a multivariate Gaussian distribution. Based on this assumption, the log-likelihood function can be further derived. The unknown parameters can be obtained by maximizing the log-likelihood function. More derivation details can be referred in Ref. [40]. After the parameters in CGP model are estimated, the nonlinear variation model can be calibrated to predict the dimensional deviations more accurately.

3 Case Study

In this section, a case study is conducted to illustrate the performance of the proposed HNVM in predicting the assembly deviation. The experiment setting and the assembly deviation are elaborated in Sec. 3.1. Then, the FEA experiment is conducted to validate the proposed model in Sec. 3.2. Finally, we compare our method with the existing methods and provide the discussions in Sec. 3.3.

3.1 Problem Description. In this section, we mainly illustrate the experiment setting and assembly deviation. The hull block is a kind of box structure [1]. In the multi-stage manufacturing process of the hull block, the welding of cantilever plates is very common. Figure 5 shows a real example of cantilever-plate welding in a ship building process. As shown in Fig. 5(a), plate 1 and plate 2 are cantilever plates of block #684, which are welded within block #684 in the first stage. Similarly, block #744 also has cantilever plates with opposite direction. In the next assembly stage, block #684 and block #744 are assembled together (as shown in Fig. 5(b)). Because of the large structural stiffness and the great weight of the block, the ends connected to the block are fixed while the ends used to weld block #684 and block #744 together are free.

In order to explain how the initial part deviation propagates and how the welding shrinkage and angular distortion affect the final assembly deviation, two cantilever plates with size $800 \times 400 \times 6 \text{ mm}^3$ are assembled together by butt-welding in this case study. The Young's modulus and Poisson's ratio of the plates are $210,000 \text{ N/mm}^2$ and 0.3 , respectively. One end of each plate is fixed, and another end of each plate is clamped by two clamps at the corner. The coordinates of these four clamps are $(40, 10)$, $(-40, 10)$, $(40, 790)$, and $(-40, 790)$, respectively. Their geometry and fixture arrangement are shown in Fig. 6. The welding direction is along the y -axis.

In this case study, we assume that there is a 1 mm deviation in z -direction at the free end of these two plates. Only the welding shrinkage in the x -direction and the angular distortion around the y -axis are considered. Under this assumption, the welding constraint (17) for the paired nodes $i + 1$ and i can be represented as ${}^e\mathbf{V}_{i+1} - {}^e\mathbf{V}_i = (\Delta u_i, 0, 0, \Delta \varphi_{x_i}, 0)^T$. Table 1 lists the x - and

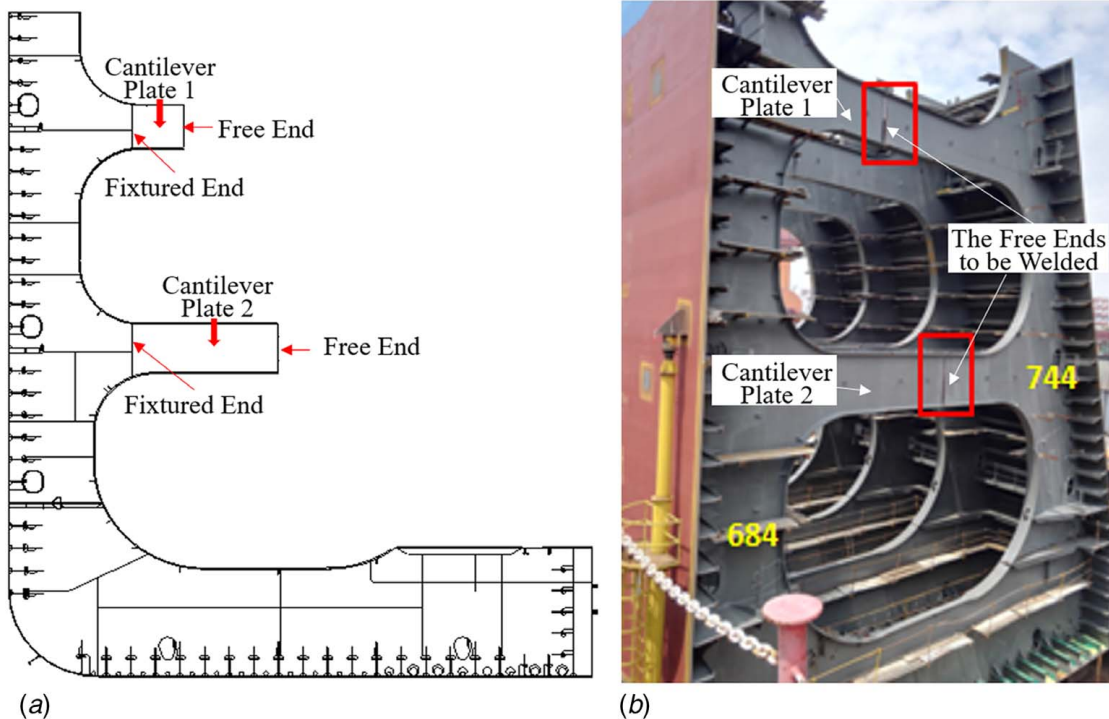


Fig. 5 An example of cantilever-plate welding in the ship building process: (a) the drawing of block #684 and (b) the assembly of block #684 and block #744

y-coordinates of the nodes where part deviation exists. The corresponding shrinkages in the x -direction and angular distortions around the y -axis are obtained from FEM simulation and also listed in Table 1. The shrinkages and angular distortions are measured after FEM simulation, which will be described in Sec. 3.2.

After the part deviation is introduced and the welding constraint is obtained, the assembly deviation of each node can be predicted by solving Eq. (18) via MATLAB. We set $\xi = 2 \times 10^{-7}$ as the convergence criteria in this case. After getting NVM, the model calibration by CGP is conducted in R “CGP” package [41]. In the model calibration, the initial value of σ^2/τ^2 is needed. In this case study, we set $\sigma^2/\tau^2 = 0.2$ as the initial value. Notably, the different initial values will not make a large difference on the final calibration results.

3.2 Finite Element Method Simulation. In this section, the parameters used in FEM simulation of welding are first provided

in Sec. 3.2.1, and then, the simulation results are shown in Sec. 3.2.2.

3.2.1 Parameter Setting. The proposed model is verified using a three-dimensional thermal-elastic-plastic FEM simulation in *Simufact.welding* 6.0.0 software. The FEM simulation procedure can be referred to in Ref. [42]. In our welding simulation, low carbon steel material (S235-SPM_sw) is selected to estimate the deformation. The material properties can be found from the material database of *Simufact.welding* 6.0.0. The double ellipsoid heat source model [43] is used. The heat source parameters of width, depth, front length, and rear length involved are 3 mm, 6 mm, 3 mm, and 6 mm, respectively. The dimensions, part deviations, and fixture arrangement for the parts are the same as illustrated in Sec. 3.1. The clamping force on each fixture is 500 N. The eight-node linear hexahedron element is used for this welding simulation. The original mesh size for the parts is $10 \times 10 \times 6 \text{ mm}^3$. However, an automatic local mesh refinement is employed on the areas of

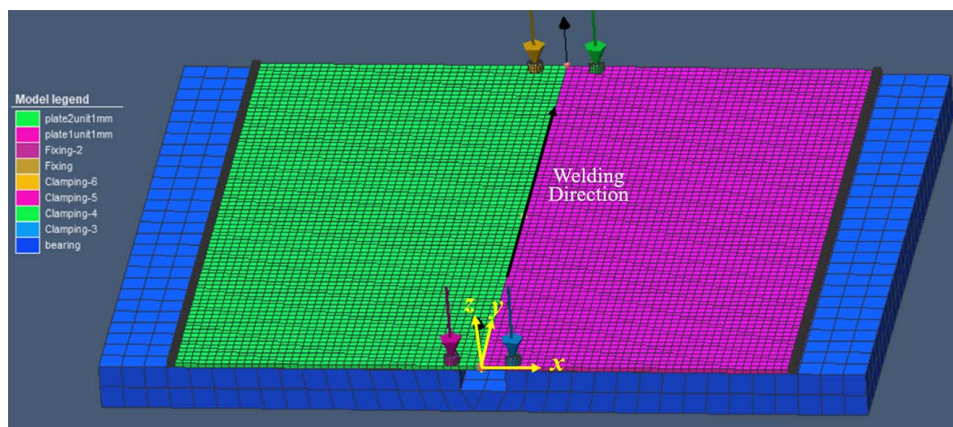


Fig. 6 The geometry and fixture arrangement for the assembly

Table 1 Part deviations, shrinkages, and angular distortions in FEM simulation

x - and y -coordinates of nodes with dimensional deviations (mm)	Part deviations in z -direction (mm)	Shrinkages in x -direction (mm)	Angular distortions around y -axis (10^{-3} rad)
(0,0)	1	-0.33	0.66
(0,50)	1	-0.50	0.17
(0,100)	1	-0.55	0.33
(0,150)	1	-0.56	0.67
(0,200)	1	-0.57	1.00
(0,250)	1	-0.57	1.33
(0,300)	1	-0.57	1.33
(0,350)	1	-0.57	1.67
(0,400)	1	-0.57	1.66
(0,450)	1	-0.57	0.67
(0,500)	1	-0.56	1.33
(0,550)	1	-0.56	1.00
(0,600)	1	-0.55	1.00
(0,650)	1	-0.54	0.67
(0,700)	1	-0.53	0.33
(0,750)	1	-0.47	0.33
(0,800)	1	-0.43	0.67

Table 2 Welding parameters

Parameters	Value
Current	250 A
Voltage	27 V
Welding speed	41.18 cm/min

welding zones to improve the simulation accuracy. Each refinement level halves the element size in the heat input area [44]. In this study, the refinement level is set as 2. Table 2 lists the welding parameters.

3.2.2 Simulation Results

- (1) *Distortion in the x -direction:* Fig. 7(a) shows the distortion in the x -direction after welding. Because both ends of the plates are fixed during the assembly, the width of the assembly is not changed. However, there are different displacements in the x -direction for the internal nodes of the assembled plates. As shown in Fig. 7(a), the distortion in the x -direction is symmetric about the y -axis and the distortion is more significant close to the weld seam, which is consistent with our equivalent treatment for the in-plane shrinkage using the penetration between the paired nodes.
- (2) *Shrinkage and Angular Distortion:* After welding, each pair of the paired nodes in FEM simulation becomes one node. Hence, it is impossible to use the paired nodes to obtain the shrinkage and angular distortion in FEM simulation. In this paper, the shrinkage in the x -direction and angular distortion around the y -axis for the weld seam are approximated from the nodes near the weld seam via the following geometry equations:

$$\Delta u_i = |x_a - x_b| - |x_{a'} - x_{b'}| \quad (23)$$

$$\Delta \varphi_{x_i} = \arccos \frac{\vec{qp} \cdot \vec{ts}}{|\vec{qp}| |\vec{ts}|} - \arccos \frac{\vec{q'p'} \cdot \vec{t's'}}{|\vec{q'p'}| |\vec{t's'}|} \quad (24)$$

where a , b , p , q , s , and t are the nodes near the weld seam. The comma superscript denotes the corresponding node before welding. x_a and x_b denote the x -coordinate values for nodes a and b after welding, respectively. $x_{a'}$ and $x_{b'}$

denote their corresponding x -coordinate values before welding. These nodes are marked in Figs. 7(b) and 7(c). Equation (23) represents the x distance change between the nodes a and b caused by welding (as shown in Fig. 7(c)). Equation (A10) represents the angle change between vector \vec{qp} and vector \vec{ts} caused by welding (as shown in Fig. 7(c)). The shrinkage in the x -direction and angular distortion around the y -axis at other positions can be obtained by the same way. Then, we can get the constraint input for our proposed model (as shown in Table 1).

- (3) *Distortion in the z -direction:* Fig. 8 shows the distortion in the z -direction after welding. As shown in Fig. 8, the z -distortion along the weld seam is significant and symmetric about the y -axis. Notably, the distortion results in FEM simulation is with respect to the initial parts with the part deviation. In order to get the deviations of the key nodes in the z -direction relative to their nominal positions, the z -coordinate values should be extracted from this FEM simulation and subtract the corresponding nominal z -coordinate values.

3.3 Results, Comparison, and Discussion. In this section, we provide comparisons and discussions to validate the proposed model. We first compare the overall assembly deviation calculated by NVM, HNVM, MIC, and FEM simulation, respectively. Then we select some locations on the plates to further illustrate the local deviation and discuss the performance of our proposed model. Finally, the central processing unit (CPU) time required for different methods is compared.

3.3.1 Overall Deviation. In order to make a comparison, we calculated the overall z -deviation for the assembly by NVM, HNVM, MIC, and FEM simulation, respectively. The deviation surface calculated by different methods is shown in Fig. 9. As shown in Fig. 9(a), the deviation surface calculated by MIC is far away from the FEM simulation while the deviation surfaces calculated by NVM and HNVM are much more consistent with the FEM simulation. In the fixtured assembly processes, the in-plane welding shrinkage results in a tension state for the assembly, which increases the out-of-plane stiffness significantly. Therefore, the spring back introduced by the part deviation is reduced. The proposed NVM and HNVM consider this fact so the results are close to the FEM simulation.

Figure 9(a) also shows that the deviation surface calculated by MIC is smooth while the FEM simulation deviation surface is not smooth at the weld seam area. The welding angular distortion around the weld seam is critical for the smoothness of the deviation surface. The welding angular distortion around the y -axis is considered by the constraint equation in NVM for this case, so there are different degrees of angular deformation for the weld seam in the NVM deviation surface. HNVM calibrates other local deviations of the assembly surface in a further step, which makes it more consistent with the FEM simulation surface. Therefore, the HNVM deviation surface almost completely overlaps with the FEM simulation surface (as shown in Fig. 9(b)).

3.3.2 Local Deviation. To further illustrate the comparison of local z -deviations, we select the nodes at $x = -50$ mm, -150 mm, -250 mm, -350 mm and $y = 0$ mm, 250 mm, 550 mm, 800 mm, respectively, which are marked by white lines in Fig. 8. The deviations of these nodes predicted by NVM, HNVM, MIC, and FEM simulation are shown in Figs. 10 and 11. According to Ref. [42], the mean error of FEM simulation in *Simufact.welding* 6.0.0 to the real experiment is less than 10%. Thus, a 10% error range is added to the FEM results. From Figs. 10 and 11, we know that the FEM error range is very small compared with the results calculated by MIC, NVM, and HNVM. Thus, the FEM simulation result has sufficient accuracy to verify our proposed model. In addition, the performance of deviation prediction by NVM is much better than MIC. The maximum error between NVM and FEM simulation is less than

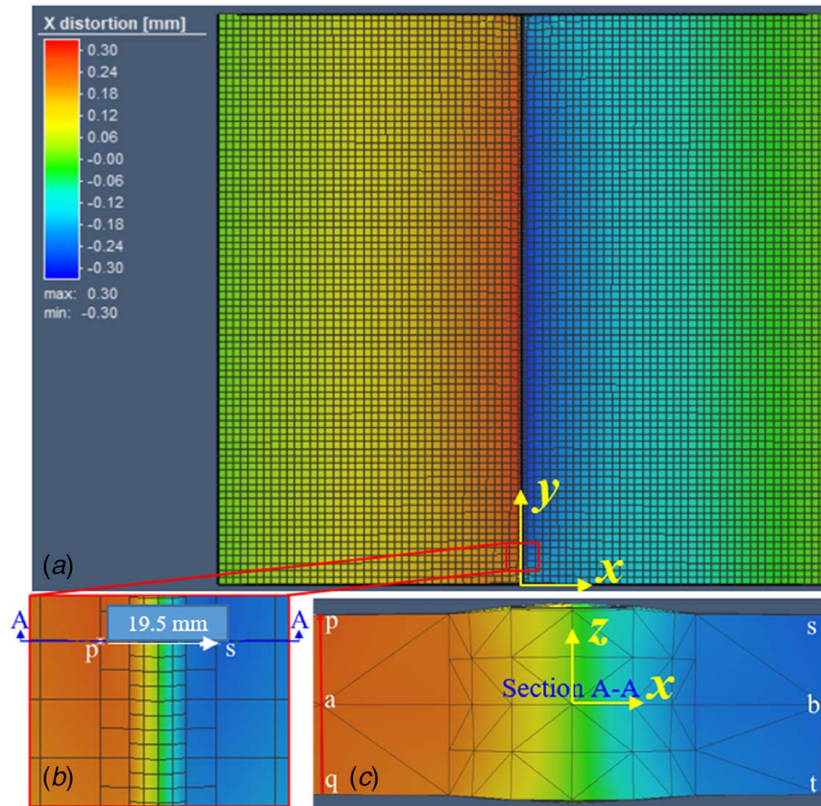


Fig. 7 Distortion after welding: (a) x distortion, (b) the measurement of shrinkage in the x-direction, and (c) the measurement of angular distortion around the y-axis

0.05 mm in these nodes. After calibration, the HNVM is in accord with the FEM simulation results very well.

Figures 10(a)–10(d) show the deviations calculated by different methods at $x = -50$ mm, -150 mm, -250 mm, and -350 mm, respectively. As shown in Fig. 10(a), the deviation at $x = -50$ mm calculated by NVM is smaller than FEM. However, the

prediction accuracy increases significantly compared with MIC. When y-coordinate value increases, the deviation calculated by FEM simulation also increases, which means the spring-back effect of the assembly increases accordingly. In fact, the welding direction will affect the final deformation of the weld seam significantly. The welding process is conducted along the y-axis, which

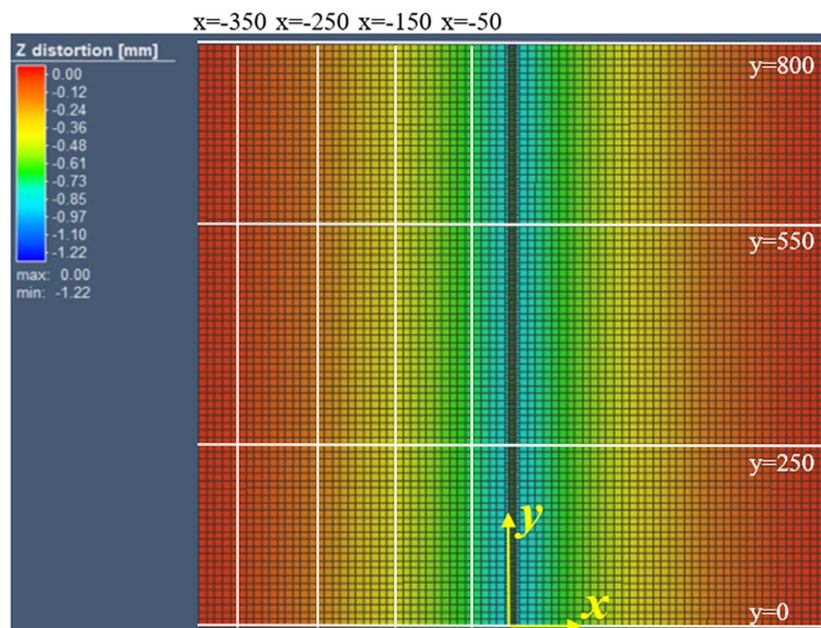


Fig. 8 Z distortion after welding

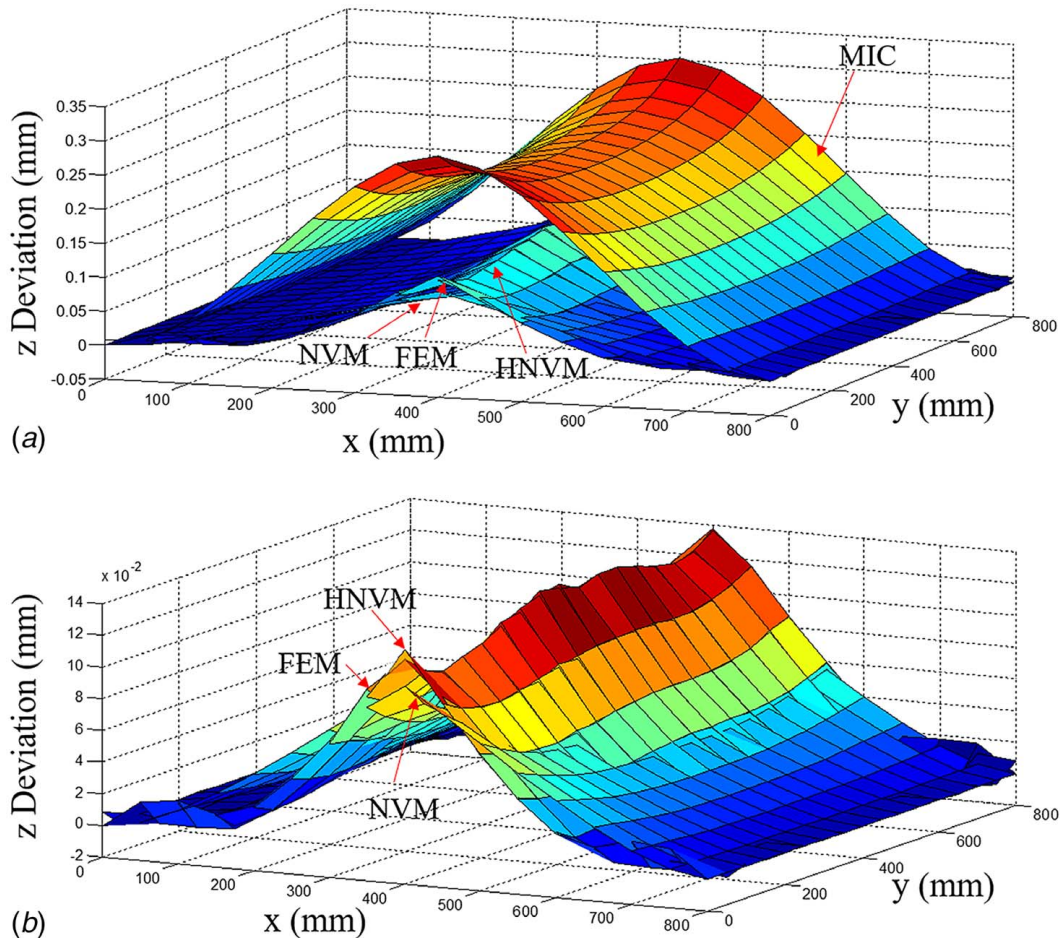


Fig. 9 Overall deviation for the assembly calculated by different methods: (a) MIC, NVM, HNVM, and FEM and (b) NVM, HNVM, and FEM

leads to a progressive solidification along the y -axis. The progressive solidification results in different angular distortion around the x -axis and makes a different restriction to the spring back of the assembly.

By comparisons between Figs. 10(a) and 10(b), we can find that the nodes that are closer to the weld seam, the increasing trend of deviation along the y -axis from the FEM method would be more obvious. This is because the progressive solidification mainly affects the assembly deviation near the weld seam. The NVM does not fully consider the progressive solidification introduced by the welding direction so the increasing trend of deviation along the y -axis is not presented. However, after calibration, the trend of the HNVM deviation surface is similar to FEM simulation. The FEM simulation results in Figs. 10(c) and 10(d) show that there are some small buckling distortions at the edge ($y=0$ mm and $y=800$ mm). This is because the welding process introduces angular distortion around the x -axis and the local y -direction shrinkage at two ends of the weld seam at the same time. These two kinds of deformations propagate to the end of the assembly and then are restricted due to the fixed end of the assembly. The restriction leads to some small buckling distortions at the edge. In our case study, the angular distortion around the x -axis is set as 0 rad and the local y -direction shrinkage at two ends of the welding seam is also ignored so the buckling distortions are not presented. At the same time, HNVM also has a difference with the FEM method in Fig. 10(d). This is because the CGP model does not consider the fixed boundary condition in calibration. However, the difference is very small (i.e., the maximum difference is less than 0.01 mm), which meets the engineering requirement and can be used in practice.

Figures 11(a)–11(d) show the deviations calculated by different methods at $y=0$ mm, 250 mm, 550 mm, and 800 mm, respectively. As shown in these four figures, the predicted deviation calculated by NVM is smaller than the FEM simulation near the weld seam. The deviation of the nodes around the weld seam is affected by elastic deformation, plastic deformation, and phase transformation deformation. In such a situation, the only shrinkage in the x -direction and the angular distortion around the y -axis cannot fully capture the assembly deviation of the weld seam, but the max error is less than 0.05 mm. Such a result means NVM has a reasonable prediction accuracy. According to the FEM simulation results shown in Figs. 11(a) and 11(d), there are some small buckling distortions at the edge of assembly where x is less than -250 mm or greater than 250 mm, which can also be found in Figs. 10(c) and 10(d). Figures 11(b) and 11(c) show that the deviation surface from the weld seam to the end of the assembly plate is very smooth and the deviation surface calculated by NVM has a similar trend with FEM in a small difference. However, the HNVM has similar results as FEM, thereby indicating the HNVM is able to predict the deviation accurately without FEM.

3.3.3 Computational Efficiency. In order to compare the computational efficiency of different methods, the CPU time required for different methods is recorded, which is shown in Table 3. The different methods are implemented at a laptop with Intel® Core™ i7-7500 CPU @ 2.70 GHz–2.90 GHz. As shown in Table 3, the CPU time required for the welding FEM simulation is more than 8 h. After the welding shrinkage and angular distortion are obtained by the welding FEM

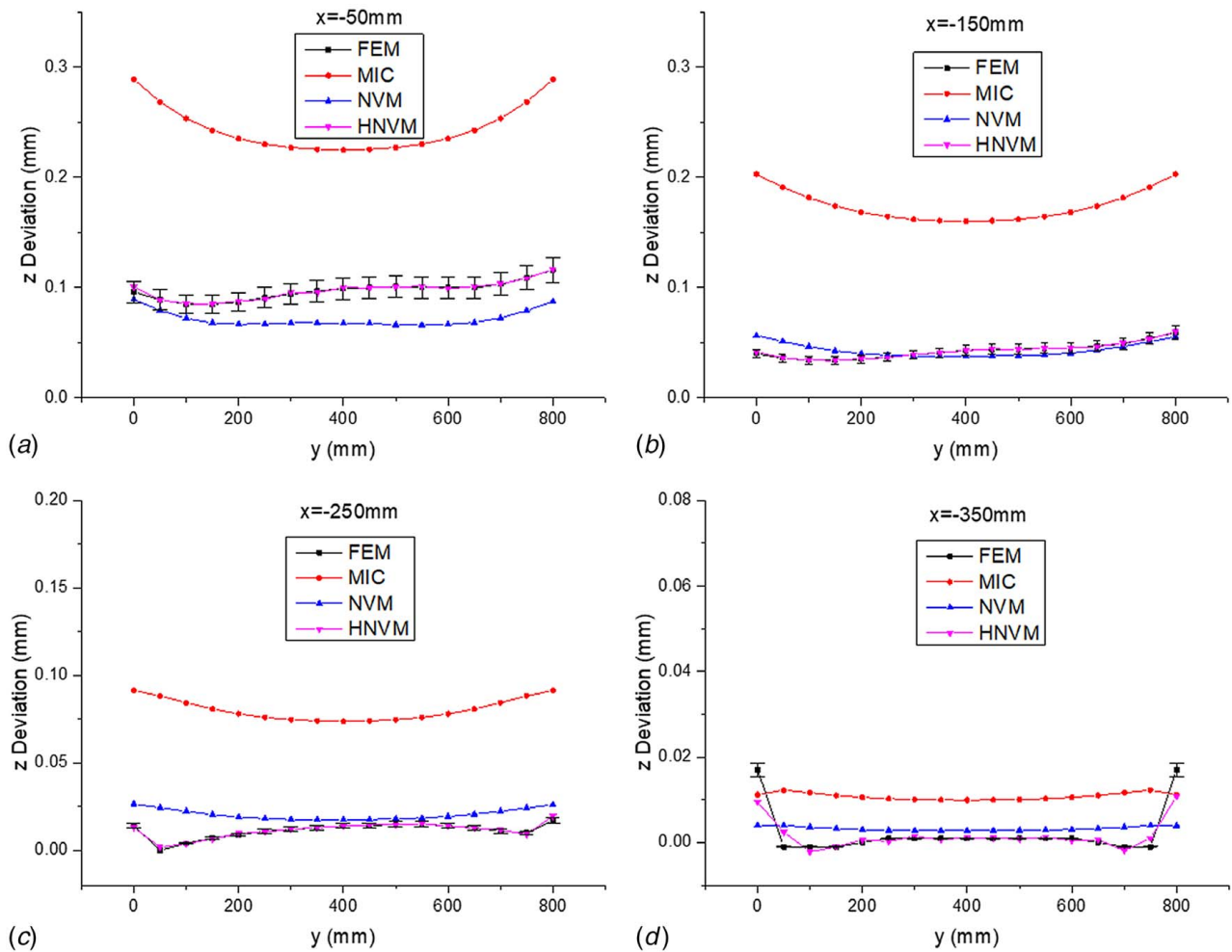


Fig. 10 The deviations calculated by different methods at lines (a) $x = -50$ mm, (b) $x = -150$ mm, (c) $x = -250$ mm, and (d) $x = -350$ mm

simulation, the CPU time required for the proposed method is only 127.77 s. By generating different part deviations, the proposed method can be employed in the statistical assembly variation analysis for the ship building process without repeated welding FEM simulations. Even though the classical MIC is the fastest method (the CPU time is only 3.98 s), it does not consider the impacts of the welding deformation and the nonlinearity, thereby leading to a relatively larger prediction error. Therefore, the proposed method is much more efficient for variation simulations of compliant metal plate assemblies considering welding shrinkage and angular distortion.

4 Conclusion

This paper developed an HNVM to predict the assembly deviation of the compliant metal plate assembly process in a single-station where welding shrinkage and angular distortion exist. The proposed model was validated by a seam-welding case, where comparisons and analysis were conducted among different methods including NVM, HNVM, MIC, and FEM simulation. The results show that the proposed model is consistent with the FEM simulation and outperforms the existing MIC in terms of the prediction of assembly deviation. Although the proposed method is validated by the plate assembly in ship hull manufacturing, it can be also applied or extended to other assembly process, which considers the geometric nonlinearity and welding deformation.

The major conclusions and contributions of this paper are summarized as follows:

- (1) This paper develops a method to consider the nonlinear mechanical behavior in the metal plate assembly process. Geometric nonlinearity has a significant influence on the out-of-plane stiffness. Based on the first-order plate theory, this paper proposes NVM, which is derived to calculate the nonlinear deviation in the releasing step. It can be degenerated to a MIC model by removing nonlinearity terms in equilibrium equations.
- (2) The developed NVM considers the influence of welding shrinkage and angular distortion on the dimensional deviation of assembly. The in-plane shrinkage and the angular distortion affect the spring back on the two-ends-fixed condition. In-plane shrinkage will significantly increase the out-of-plane stiffness and reduce the assembly deviation. However, the angular distortion, especially the angular distortion around the weld seam, will increase the assembly deviation. In this paper, we proposed a welding constraint equation by modifying the matching criteria of the paired nodes to make the welding deformation as a constraint condition for the assembly. Notably, the proposed method avoids a great amount of FEM simulations by incorporating welding deformations as parameters in the model.
- (3) The HNVM leads to further improvements in the prediction accuracy of assembly deviation. With the help from the

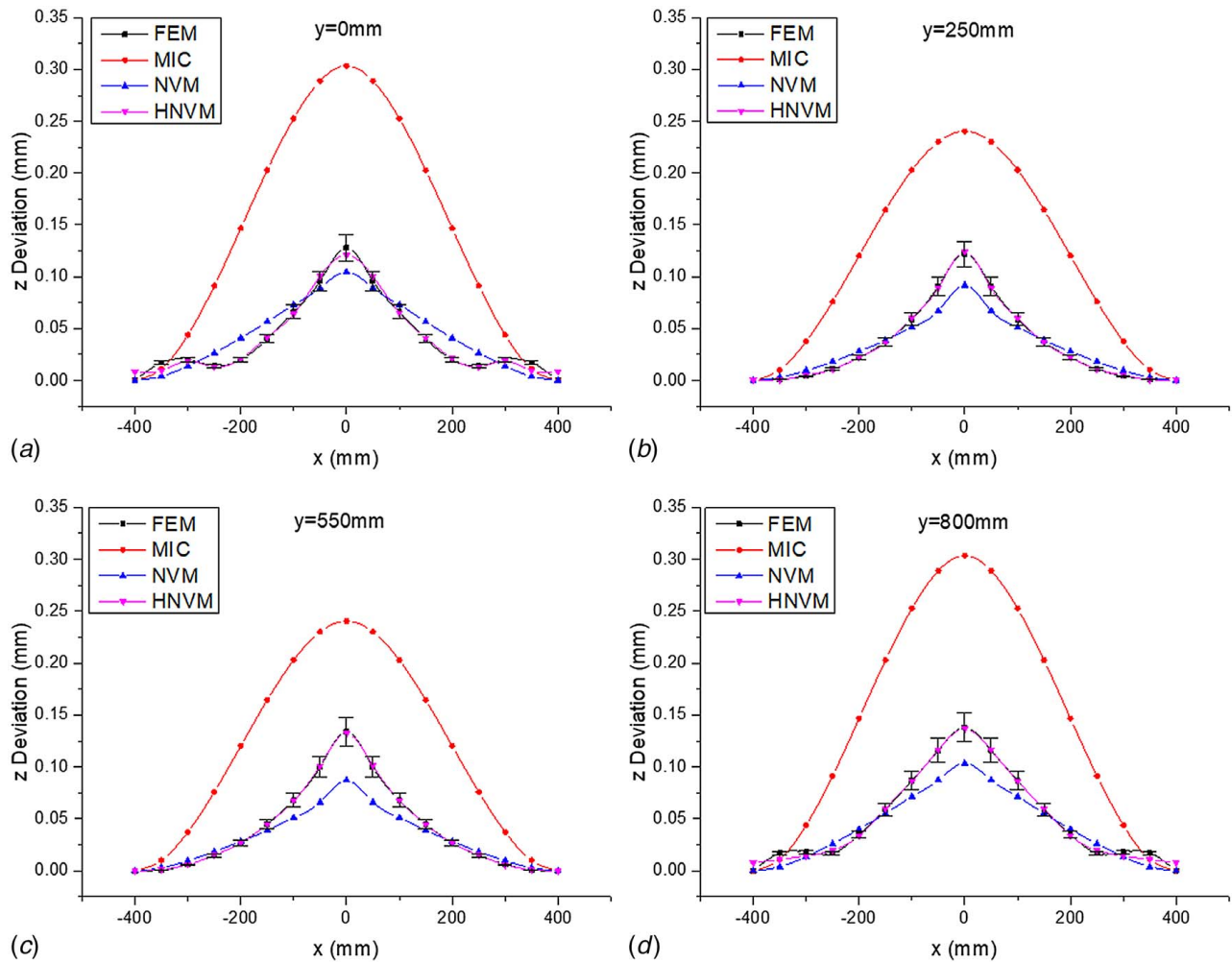


Fig. 11 The deviations calculated by different methods at lines (a) $y = 0$ mm, (b) $y = 250$ mm, (c) $y = 550$ mm, and (d) $y = 800$ mm

Table 3 CPU time for different methods

Methods	CPU time (seconds)
Welding FEM simulation	29,000
MIC	3.98
HNVM	127.77

calibration using CGP model, the HNVM can capture the local deviations induced by other factors near the weld seam. After calibration, the HNVM is finally established, which can be used to conduct deterministic and statistical assembly variation analysis for the welding process of metal plate assemblies.

The proposed modeling and analysis method has several potential improvements in the future. Associate with geometric variation, the levels of assembly stresses are also very important variables in the shipbuilding process. As dimensional variation propagates along the multi-stage assembly process, the residual stresses will also be accumulated, which will further have impacts on the structural reliability and sustainability of the ship. Thus, how to conduct stress modeling and analysis is an important future work for multi-stage ship building process. In addition, fixture position errors are not considered in this study, which also deserves further investigations for the influence on the welding distortion.

Acknowledgment

This work was partially supported by the Ministry of Industry and Information Technology of the People's Republic of China (Grant No. MC-201720-Z02), National Science and Technology Major Project (Grant No. 2017-VII-0008-0102), and China Post-doctoral Science Foundation (Grant No. 17Z102060069).

Nomenclature

- e = element
- i = number of a node
- m = the total number of constraints
- n = iterations
- A = assembly
- C = calibration
- M = the total number of nodes
- P = part
- d = the displacement constraint vector
- F_{\odot} = clamping force vector or releasing force vector, $\odot \in \{clamp, release\}$
- ${}^e F$ = element external force vector
- G = coefficient matrix for the constraint equation
- K_{clamp} = the total stiffness matrix of parts in clamping process
- K_L = the linear term (L) of $K_S({}^A V)$
- $K_S({}^A V)$ = the secant stiffness that is related to the assembly deviation
- $K_{N1}({}^A V)$ = the first-order nonlinear item of $K_S({}^A V)$

- $\mathbf{K}_{N2}({}^A\mathbf{V})$ = the second-order nonlinear item of $\mathbf{K}_S({}^A\mathbf{V})$
- \mathbf{K}_s^n = the secant stiffness matrix in the n th iteration
- \mathbf{K}_T^n = the tangent stiffness matrix in the n th iteration
- ${}^e\mathbf{K}_S({}^e\mathbf{V})$ = the element nonlinear secant stiffness matrix
- ${}^e\mathbf{K}_T({}^e\mathbf{V})$ = the element nonlinear tangent stiffness matrix
- ${}^e\mathbf{K}_L$ = the linear term (L) of ${}^e\mathbf{K}_S({}^e\mathbf{V})$
- ${}^e\mathbf{K}_{N1}({}^e\mathbf{V})$ = the first-order nonlinear item of ${}^e\mathbf{K}_S({}^e\mathbf{V})$
- ${}^e\mathbf{K}_{N2}({}^e\mathbf{V})$ = the second-order nonlinear item of ${}^e\mathbf{K}_S({}^e\mathbf{V})$
- ${}^x\mathbf{V}$ = the variation vector of \mathbf{x} , $\mathbf{x} \in \{A, P, P_1, P_2\}$
- ${}^A\mathbf{V}^*$ = the final variation vector of assembly
- $\Delta^A\mathbf{V}$ = the first order of the increment deviation
- $\Delta^A\mathbf{V}^n$ = the first order of the increment deviation in the n th iteration
- ${}^e\mathbf{V}$ = the element displacement vector
- ${}^e\mathbf{V}_i$ = the displacement vector of i th node
- u_0 = the deformation of a point at the referential mid-plane in x -direction
- w_0 = the deformation of a point at the referential mid-plane in z -direction
- x_\bullet = the x -coordinate values for the node \bullet in the FEM simulation model, and $\bullet \in \{a, a', b, b'\}$
- $P_\#$ = the $\#$ th part. $\# \in \{1, 2\}$
- ${}^C\mathbf{V}$ = the variation in z -direction after calibration for a node
- $g(x, y)$ = the correlation structure of GP for modeling global variations in CGP model
- $l(x, y)$ = the correlation structure of GP for modeling local variations in CGP model
- δ = the model error to be calibrated by CGP model for a node
- Δu_i = the equivalent relative displacement in x -direction for the paired nodes $i + 1$ and i
- Δv_i = the equivalent relative displacement in y -direction for the paired nodes $i + 1$ and i
- Δw_i = the equivalent relative displacement in z -direction for the paired nodes $i + 1$ and i
- $\Delta \varphi_{xi}$ = the equivalent relative angular distortion around y -axis for the paired nodes $i + 1$ and i
- $\Delta \varphi_{yi}$ = the equivalent relative angular distortion around x -axis for the paired nodes $i + 1$ and i
- ${}^e\Delta_i$ = the equivalent relative displacement for the paired nodes $i + 1$ and i
- $\theta(X)$ = the standardized volatility function
- λ = the Lagrange multiplier
- μ = the constant mean of the global variation in CGP model
- ξ = the convergence criteria
- σ^2 = constant variance
- $\sigma^2(x, y)$ = the variance function of the local variation in CGP model
- τ^2 = variance of the global variation in CGP model
- v_0 = the deformation of a point at the referential mid-plane in y -direction

- φ_x = the rotation angles of normal to the cross section with respect to y -axis
- φ_y = the rotation angles of normal to the cross section with respect to x -axis

Appendix: Derivation of Element's Nonlinear Secant Stiffness Matrix

Taking a rectangle plate with uniform thickness h as an example (shown in Fig. 12). For any element, the Eq. (12) can be expanded as

$$\begin{bmatrix} {}^e k_{11} & {}^e k_{12} & {}^e k_{13} & {}^e k_{14} & {}^e k_{15} \\ {}^e k_{21} & {}^e k_{22} & {}^e k_{23} & {}^e k_{24} & {}^e k_{25} \\ {}^e k_{31} & {}^e k_{32} & {}^e k_{33} & {}^e k_{34} & {}^e k_{35} \\ {}^e k_{41} & {}^e k_{42} & {}^e k_{43} & {}^e k_{44} & {}^e k_{45} \\ {}^e k_{51} & {}^e k_{52} & {}^e k_{53} & {}^e k_{54} & {}^e k_{55} \end{bmatrix} \begin{bmatrix} u_0 \\ v_0 \\ w_0 \\ \phi_x \\ \phi_y \end{bmatrix} = \begin{bmatrix} {}^e F_1 \\ {}^e F_2 \\ {}^e F_3 \\ {}^e F_4 \\ {}^e F_5 \end{bmatrix} \quad (A1)$$

where ${}^e F_1, {}^e F_2, {}^e F_3, {}^e F_4, {}^e F_5$ are external force components of the element.

When the ratio of thickness to length and width is less than 1:50, the rotation angles of normal to the cross section about the y - and the x -axes caused by in-plane deformation can be written as

$$\varphi_x \rightarrow -\frac{\partial w_0}{\partial x}, \quad \varphi_y \rightarrow -\frac{\partial w_0}{\partial y} \quad (A2)$$

According to the *von Kármán* plate theory, the strains for the displacement field are shown as

$$\begin{aligned} \epsilon_{xx} &= \frac{\partial u_0}{\partial x} + \frac{1}{2} \left(\frac{\partial w_0}{\partial x} \right)^2 + z \frac{\partial \varphi_x}{\partial x} \\ \epsilon_{yy} &= \frac{\partial v_0}{\partial y} + \frac{1}{2} \left(\frac{\partial w_0}{\partial y} \right)^2 + z \frac{\partial \varphi_y}{\partial y} \\ \epsilon_{zz} &= 0 \\ \gamma_{xy} &= \left(\frac{\partial u_0}{\partial y} + \frac{\partial v_0}{\partial x} + \frac{\partial w_0}{\partial x} \frac{\partial w_0}{\partial y} \right) + z \left(\frac{\partial \varphi_x}{\partial y} + \frac{\partial \varphi_y}{\partial x} \right) \\ \gamma_{xz} &= \frac{\partial w_0}{\partial x} + \varphi_x \\ \gamma_{yz} &= \frac{\partial w_0}{\partial y} + \varphi_y \end{aligned} \quad (A3)$$

Let $\bar{u}_0, \bar{v}_0, \bar{w}_0, \bar{\varphi}_x,$ and $\bar{\varphi}_y$ denote the initial displacement field; $\tilde{u}_0, \tilde{v}_0, \tilde{w}_0, \tilde{\varphi}_x,$ and $\tilde{\varphi}_y$ denote the final displacement field; and $u_0,$

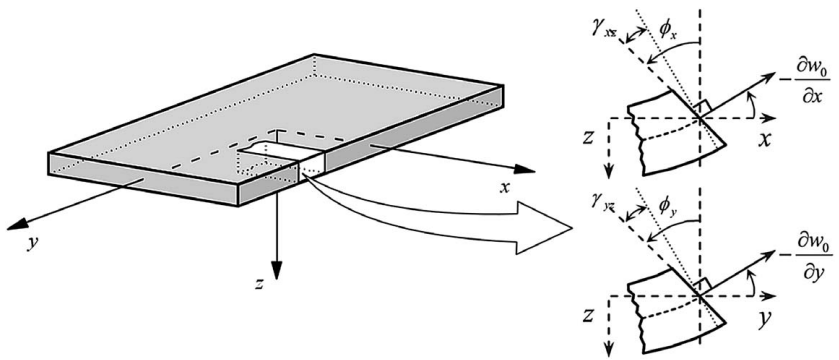


Fig. 12 Undeformed and deformed geometries of an element of a plate in the Mindlin theory

v_0 , w_0 , φ_x , and φ_y denote displacement increments caused by the external forces; then we have

$$\begin{aligned}
 \tilde{\epsilon}_{xx} - \bar{\epsilon}_{xx} &= \left[\frac{\partial \tilde{u}_0}{\partial x} + \frac{1}{2} \left(\frac{\partial \tilde{w}_0}{\partial x} \right)^2 + z \frac{\partial \tilde{\varphi}_x}{\partial x} \right] - \left[\frac{\partial \bar{u}_0}{\partial x} + \frac{1}{2} \left(\frac{\partial \bar{w}_0}{\partial x} \right)^2 + z \frac{\partial \bar{\varphi}_x}{\partial x} \right] \\
 \tilde{\epsilon}_{yy} - \bar{\epsilon}_{yy} &= \left[\frac{\partial \tilde{v}_0}{\partial y} + \frac{1}{2} \left(\frac{\partial \tilde{w}_0}{\partial y} \right)^2 + z \frac{\partial \tilde{\varphi}_y}{\partial y} \right] - \left[\frac{\partial \bar{v}_0}{\partial y} + \frac{1}{2} \left(\frac{\partial \bar{w}_0}{\partial y} \right)^2 + z \frac{\partial \bar{\varphi}_y}{\partial y} \right] \\
 \tilde{\epsilon}_{zz} - \bar{\epsilon}_{zz} &= 0 \\
 \tilde{\gamma}_{xy} - \bar{\gamma}_{xy} &= \left[\left(\frac{\partial \tilde{u}_0}{\partial y} + \frac{\partial \tilde{v}_0}{\partial x} + \frac{\partial \tilde{w}_0}{\partial x} \frac{\partial \tilde{w}_0}{\partial y} \right) + z \left(\frac{\partial \tilde{\varphi}_x}{\partial y} + \frac{\partial \tilde{\varphi}_y}{\partial x} \right) \right] - \left[\left(\frac{\partial \bar{u}_0}{\partial y} + \frac{\partial \bar{v}_0}{\partial x} + \frac{\partial \bar{w}_0}{\partial x} \frac{\partial \bar{w}_0}{\partial y} \right) + z \left(\frac{\partial \bar{\varphi}_x}{\partial y} + \frac{\partial \bar{\varphi}_y}{\partial x} \right) \right] \\
 \tilde{\gamma}_{xz} - \bar{\gamma}_{xz} &= \left[\frac{\partial \tilde{w}_0}{\partial x} + \tilde{\varphi}_x \right] - \left[\frac{\partial \bar{w}_0}{\partial x} + \bar{\varphi}_x \right] \\
 \tilde{\gamma}_{yz} - \bar{\gamma}_{yz} &= \left[\frac{\partial \tilde{w}_0}{\partial y} + \tilde{\varphi}_y \right] - \left[\frac{\partial \bar{w}_0}{\partial y} + \bar{\varphi}_y \right]
 \end{aligned} \tag{A4}$$

The virtual strain energy is given by:

$$\delta \Pi = \int_{\Omega} \left\{ \int_{-h/2}^{h/2} \left[\sigma_{xx} \delta \tilde{\epsilon}_{xx} + \sigma_{yy} \delta \tilde{\epsilon}_{yy} + \sigma_{xy} \delta \tilde{\gamma}_{xy} + S \sigma_{xz} \delta \tilde{\gamma}_{xz} + S \sigma_{yz} \delta \tilde{\gamma}_{yz} \right] dz \right\} dx dy \tag{A5}$$

where the shear correction factor S is introduced to account for the state of shear stress through thickness based on the first-order plate theory (*Mindlin theory*).

Suppose that

$$\begin{Bmatrix} N_{xx} \\ N_{yy} \\ N_{xy} \end{Bmatrix} = \int_{-h/2}^{h/2} \begin{Bmatrix} \sigma_{xx} \\ \sigma_{yy} \\ \sigma_{xy} \end{Bmatrix} dz, \quad \begin{Bmatrix} M_{xx} \\ M_{yy} \\ M_{xy} \end{Bmatrix} = \int_{-h/2}^{h/2} z \begin{Bmatrix} \sigma_{xx} \\ \sigma_{yy} \\ \sigma_{xy} \end{Bmatrix} dz, \quad \begin{Bmatrix} Q_x \\ Q_y \end{Bmatrix} = S \int_{-h/2}^{h/2} \begin{Bmatrix} \sigma_{xz} \\ \sigma_{yz} \end{Bmatrix} dz \tag{A6}$$

Then, Eq. (A5) can be rewritten as

$$\delta \Pi = \int_{\Omega} \left(N_{xx} \delta \tilde{\epsilon}_{xx}^0 + N_{yy} \delta \tilde{\epsilon}_{yy}^0 + N_{xy} \delta \tilde{\gamma}_{xy}^0 + M_{xx} \delta \tilde{\epsilon}_{xx}^1 + M_{yy} \delta \tilde{\epsilon}_{yy}^1 + M_{xy} \delta \tilde{\gamma}_{xy}^1 + Q_x \delta \tilde{\gamma}_{xz}^0 + Q_y \delta \tilde{\gamma}_{yz}^0 \right) dx dy \tag{A7}$$

Substituting Eq. (A4) into Eq. (A7), we have

$$\begin{aligned}
 \delta \Pi &= - \int_{\Omega} \delta \tilde{u}_0 \left(\frac{\partial N_{xx}}{\partial x} + \frac{\partial N_{xy}}{\partial y} \right) dx dy - \int_{\Omega} \delta \tilde{v}_0 \left(\frac{\partial N_{yy}}{\partial y} + \frac{\partial N_{xy}}{\partial x} \right) dx dy \\
 &\quad - \int_{\Omega} \delta \tilde{w}_0 \left[\left(\frac{\partial Q_x}{\partial x} + \frac{\partial Q_y}{\partial y} \right) + \frac{\partial}{\partial x} \left(N_{xx} \frac{\partial \tilde{w}_0}{\partial x} + N_{xy} \frac{\partial \tilde{w}_0}{\partial y} \right) + \frac{\partial}{\partial y} \left(N_{xy} \frac{\partial \tilde{w}_0}{\partial x} + N_{yy} \frac{\partial \tilde{w}_0}{\partial y} \right) \right] dx dy \\
 &\quad - \int_{\Omega} \delta \tilde{\varphi}_x \left(\frac{\partial M_{xx}}{\partial x} + \frac{\partial M_{xy}}{\partial y} - Q_x \right) dx dy - \int_{\Omega} \delta \tilde{\varphi}_y \left(\frac{\partial M_{yy}}{\partial y} + \frac{\partial M_{xy}}{\partial x} - Q_y \right) dx dy \\
 &\quad + \int_{-L_a/2}^{L_a/2} \left\{ \left[N_{yy} \delta \tilde{u}_0 + N_{xy} \delta \tilde{v}_0 + \left(N_{yy} \frac{\partial \tilde{w}_0}{\partial y} + N_{xy} \frac{\partial \tilde{w}_0}{\partial x} + Q_y \right) \delta \tilde{w}_0 + M_{xy} \delta \tilde{\varphi}_x + M_{yy} \delta \tilde{\varphi}_y \right] \Big|_{-L_b/2}^{L_b/2} \right\} dx \\
 &\quad + \int_{-L_b/2}^{L_b/2} \left\{ \left[N_{xx} \delta \tilde{u}_0 + N_{xy} \delta \tilde{v}_0 + \left(N_{xx} \frac{\partial \tilde{w}_0}{\partial x} + N_{xy} \frac{\partial \tilde{w}_0}{\partial y} + Q_x \right) \delta \tilde{w}_0 + M_{xx} \delta \tilde{\varphi}_x + M_{xy} \delta \tilde{\varphi}_y \right] \Big|_{-L_a/2}^{L_a/2} \right\} dy
 \end{aligned} \tag{A8}$$

For isotropic materials, the generalized *Hooke's law* relates the six components of stress to the six components of strain as:

$$\begin{Bmatrix} \sigma_{xx} \\ \sigma_{yy} \\ \sigma_{zz} \\ \sigma_{yz} \\ \sigma_{xz} \\ \sigma_{xy} \end{Bmatrix} = \begin{bmatrix} C_{11} & C_{12} & C_{12} & & & \\ C_{12} & C_{11} & C_{12} & & & \\ C_{12} & C_{12} & C_{11} & & & \\ & & & C_{44} & & \\ & & & & C_{44} & \\ & & & & & C_{44} \end{bmatrix} \begin{Bmatrix} \tilde{\epsilon}_{xx} - \bar{\epsilon}_{xx} \\ \tilde{\epsilon}_{yy} - \bar{\epsilon}_{yy} \\ \tilde{\epsilon}_{zz} - \bar{\epsilon}_{zz} \\ \tilde{\gamma}_{yz} - \bar{\gamma}_{yz} \\ \tilde{\gamma}_{xz} - \bar{\gamma}_{xz} \\ \tilde{\gamma}_{xy} - \bar{\gamma}_{xy} \end{Bmatrix} \tag{A9}$$

where $C_{11} = E/(1 - \nu^2)$, $C_{12} = \nu E/(1 - \nu^2)$, $C_{44} = E/(2(1 + \nu))$ are the elastic coefficients.

The equations of equilibrium of the first-order shear deformation plate theory [38] are given by

$$\begin{aligned}
 -\left(\frac{\partial N_{xx}}{\partial x} + \frac{\partial N_{xy}}{\partial y}\right) &= 0 \\
 -\left(\frac{\partial N_{xy}}{\partial x} + \frac{\partial N_{yy}}{\partial y}\right) &= 0 \\
 -\left(\frac{\partial Q_x}{\partial x} + \frac{\partial Q_y}{\partial y}\right) - \mathfrak{N}(u_0, v_0, w_0) - q &= 0 \\
 -\left(\frac{\partial M_{xx}}{\partial x} + \frac{\partial M_{xy}}{\partial y}\right) + Q_x &= 0 \\
 -\left(\frac{\partial M_{xy}}{\partial x} + \frac{\partial M_{yy}}{\partial y}\right) + Q_y &= 0
 \end{aligned} \tag{A10}$$

where

$$\begin{aligned}
 \begin{bmatrix} N_{xx} \\ N_{yy} \\ N_{xy} \end{bmatrix} &= \begin{bmatrix} A_{11} & A_{12} & 0 \\ A_{12} & A_{22} & 0 \\ 0 & 0 & A_{66} \end{bmatrix} \\
 &\times \begin{bmatrix} \frac{\partial \tilde{u}_0}{\partial x} + \frac{1}{2} \left(\frac{\partial \tilde{w}_0}{\partial x}\right)^2 - \frac{\partial \tilde{u}_0}{\partial x} - \frac{1}{2} \left(\frac{\partial \tilde{w}_0}{\partial x}\right)^2 \\ \frac{\partial \tilde{v}_0}{\partial y} + \frac{1}{2} \left(\frac{\partial \tilde{w}_0}{\partial y}\right)^2 - \frac{\partial \tilde{v}_0}{\partial y} - \frac{1}{2} \left(\frac{\partial \tilde{w}_0}{\partial y}\right)^2 \\ \frac{\partial \tilde{u}_0}{\partial y} + \frac{\partial \tilde{v}_0}{\partial x} + \frac{\partial \tilde{w}_0}{\partial x} \frac{\partial \tilde{w}_0}{\partial y} - \frac{\partial \tilde{u}_0}{\partial y} - \frac{\partial \tilde{v}_0}{\partial x} - \frac{\partial \tilde{w}_0}{\partial x} \frac{\partial \tilde{w}_0}{\partial y} \end{bmatrix}
 \end{aligned} \tag{A11}$$

$$\begin{aligned}
 \begin{bmatrix} M_{xx} \\ M_{yy} \\ M_{xy} \end{bmatrix} &= \begin{bmatrix} D_{11} & D_{12} & 0 \\ D_{12} & D_{22} & 0 \\ 0 & 0 & D_{66} \end{bmatrix} \begin{bmatrix} \frac{\partial \tilde{\varphi}_x}{\partial x} - \frac{\partial \tilde{\varphi}_x}{\partial x} \\ \frac{\partial \tilde{\varphi}_y}{\partial y} - \frac{\partial \tilde{\varphi}_y}{\partial y} \\ \frac{\partial \tilde{\varphi}_x}{\partial y} + \frac{\partial \tilde{\varphi}_y}{\partial x} - \frac{\partial \tilde{\varphi}_x}{\partial y} - \frac{\partial \tilde{\varphi}_y}{\partial x} \end{bmatrix}
 \end{aligned} \tag{A12}$$

$$\begin{aligned}
 \begin{bmatrix} Q_y \\ Q_x \end{bmatrix} &= S \begin{bmatrix} A_{44} & 0 \\ 0 & A_{55} \end{bmatrix} \begin{bmatrix} \frac{\partial \tilde{w}_0}{\partial y} + \tilde{\varphi}_y - \frac{\partial \tilde{w}_0}{\partial y} - \tilde{\varphi}_y \\ \frac{\partial \tilde{w}_0}{\partial x} + \tilde{\varphi}_x - \frac{\partial \tilde{w}_0}{\partial x} - \tilde{\varphi}_x \end{bmatrix}
 \end{aligned} \tag{A13}$$

$$\begin{aligned}
 \mathfrak{N}(\tilde{u}_0, \tilde{v}_0, \tilde{w}_0) &= \frac{\partial}{\partial x} \left(N_{xx} \frac{\partial \tilde{w}_0}{\partial x} + N_{xy} \frac{\partial \tilde{w}_0}{\partial y} \right) \\
 &+ \frac{\partial}{\partial y} \left(N_{xy} \frac{\partial \tilde{w}_0}{\partial x} + N_{yy} \frac{\partial \tilde{w}_0}{\partial y} \right)
 \end{aligned} \tag{A14}$$

For isotropic materials with elastic modulus E , shear modulus G , and Poisson ratio ν , the extensional stiffness coefficients A_{jl} ($j=1, 2, 4, 5, 6; l=1, 2, 4, 5, 6$) and the bending stiffness coefficients D_{jl} ($j=1, 2, 6; l=1, 2, 6$) are given by Eqs. (A15) and (A16)

$$\begin{aligned}
 A_{11} = \frac{Eh}{1-\nu^2}, \quad A_{12} = \frac{\nu Eh}{1-\nu^2}, \quad A_{22} = \frac{Eh}{1-\nu^2}, \\
 A_{44} = Gh, \quad A_{55} = Gh, \quad A_{66} = Gh
 \end{aligned} \tag{A15}$$

$$\begin{aligned}
 D_{11} = \frac{Eh^3}{12(1-\nu^2)}, \quad D_{12} = \frac{\nu Eh^3}{12(1-\nu^2)}, \\
 D_{22} = \frac{Eh^3}{12(1-\nu^2)}, \quad D_{66} = \frac{Gh^3}{12}
 \end{aligned} \tag{A16}$$

The interpolations for final deformations assumed yielding to the equations of node displacements and shape functions, which can be expressed as

$$\begin{aligned}
 \tilde{u}_0(x, y) &= H_1 e^{\tilde{\mathbf{V}}} \\
 \tilde{v}_0(x, y) &= H_2 e^{\tilde{\mathbf{V}}} \\
 \tilde{w}_0(x, y) &= H_3 e^{\tilde{\mathbf{V}}} \\
 \tilde{\varphi}_x(x, y) &= H_4 e^{\tilde{\mathbf{V}}} \\
 \tilde{\varphi}_y(x, y) &= H_5 e^{\tilde{\mathbf{V}}}
 \end{aligned} \tag{A17}$$

where $e^{\tilde{\mathbf{V}}} = [\tilde{u}_0, \tilde{v}_0, \tilde{w}_0, \tilde{\varphi}_x, \tilde{\varphi}_y]^T$ is the final node deformation vector, and H_j ($j=1, 2, 3, 4, 5$) is the shape function. Then the components of element stiffness matrix are listed as

$$\begin{aligned}
 {}^e k_{11} &= \iint A_{11} \frac{\partial H_1^T}{\partial x} \frac{\partial H_1}{\partial x} dx dy + \iint A_{66} \frac{\partial H_1^T}{\partial y} \frac{\partial H_1}{\partial y} dx dy \\
 {}^e k_{12} &= \iint A_{12} \frac{\partial H_1^T}{\partial x} \frac{\partial H_2}{\partial y} dx dy + \iint A_{66} \frac{\partial H_1^T}{\partial y} \frac{\partial H_2}{\partial x} dx dy \\
 {}^e k_{13} &= \frac{1}{2} \iint A_{11} \frac{\partial w_0}{\partial x} \frac{\partial H_1^T}{\partial x} \frac{\partial H_3}{\partial x} dx dy + \frac{1}{2} \iint A_{12} \frac{\partial w_0}{\partial y} \frac{\partial H_1^T}{\partial x} \frac{\partial H_3}{\partial y} dx dy \\
 &+ \frac{1}{2} \iint A_{66} \frac{\partial w_0}{\partial x} \frac{\partial H_1^T}{\partial y} \frac{\partial H_3}{\partial y} dx dy + \frac{1}{2} \iint A_{66} \frac{\partial w_0}{\partial y} \frac{\partial H_1^T}{\partial y} \frac{\partial H_3}{\partial x} dx dy \\
 {}^e k_{14} &= 0 \\
 {}^e k_{15} &= 0 \\
 {}^e k_{21} &= \iint A_{12} \frac{\partial H_2^T}{\partial y} \frac{\partial H_1}{\partial x} dx dy + \iint A_{66} \frac{\partial H_2^T}{\partial x} \frac{\partial H_1}{\partial y} dx dy \\
 {}^e k_{22} &= \iint A_{22} \frac{\partial H_2^T}{\partial y} \frac{\partial H_2}{\partial y} dx dy + \iint A_{66} \frac{\partial H_2^T}{\partial x} \frac{\partial H_2}{\partial x} dx dy \\
 {}^e k_{23} &= \frac{1}{2} \iint A_{12} \frac{\partial w_0}{\partial x} \frac{\partial H_2^T}{\partial y} \frac{\partial H_3}{\partial x} dx dy + \frac{1}{2} \iint A_{22} \frac{\partial w_0}{\partial y} \frac{\partial H_2^T}{\partial y} \frac{\partial H_3}{\partial y} dx dy \\
 &+ \frac{1}{2} \iint A_{66} \frac{\partial w_0}{\partial y} \frac{\partial H_2^T}{\partial x} \frac{\partial H_3}{\partial x} dx dy + \frac{1}{2} \iint A_{66} \frac{\partial w_0}{\partial x} \frac{\partial H_2^T}{\partial x} \frac{\partial H_3}{\partial y} dx dy \\
 {}^e k_{24} &= 0 \\
 {}^e k_{25} &= 0 \\
 {}^e k_{31} &= \frac{1}{2} \iint A_{11} \frac{\partial w_0}{\partial x} \frac{\partial H_3^T}{\partial x} \frac{\partial H_1}{\partial x} dx dy + \frac{1}{2} \iint A_{12} \frac{\partial w_0}{\partial y} \frac{\partial H_3^T}{\partial y} \frac{\partial H_1}{\partial x} dx dy \\
 &+ \frac{1}{2} \iint A_{66} \frac{\partial w_0}{\partial x} \frac{\partial H_3^T}{\partial y} \frac{\partial H_1}{\partial y} dx dy + \frac{1}{2} \iint A_{66} \frac{\partial w_0}{\partial y} \frac{\partial H_3^T}{\partial x} \frac{\partial H_1}{\partial x} dx dy \\
 {}^e k_{32} &= \frac{1}{2} \iint A_{12} \frac{\partial w_0}{\partial x} \frac{\partial H_3^T}{\partial x} \frac{\partial H_2}{\partial y} dx dy + \frac{1}{2} \iint A_{22} \frac{\partial w_0}{\partial y} \frac{\partial H_3^T}{\partial y} \frac{\partial H_2}{\partial y} dx dy \\
 &+ \frac{1}{2} \iint A_{66} \frac{\partial w_0}{\partial y} \frac{\partial H_3^T}{\partial x} \frac{\partial H_2}{\partial x} dx dy + \frac{1}{2} \iint A_{66} \frac{\partial w_0}{\partial x} \frac{\partial H_3^T}{\partial x} \frac{\partial H_2}{\partial x} dx dy
 \end{aligned}$$

$$\begin{aligned}
{}^e k_{33} &= \iint \frac{\partial H_3^T}{\partial x} \left\{ \frac{A_{11}}{2} \left[\frac{\partial u_0}{\partial x} + \left(\frac{\partial w_0}{\partial x} \right)^2 \right] + \frac{A_{12}}{2} \left[\frac{\partial v_0}{\partial y} + \left(\frac{\partial w_0}{\partial y} \right)^2 \right] \right\} \frac{\partial H_3}{\partial x} dx dy \\
&+ \iint \frac{\partial H_3^T}{\partial y} \left\{ \frac{A_{12}}{2} \left[\frac{\partial u_0}{\partial x} + \left(\frac{\partial w_0}{\partial x} \right)^2 \right] + \frac{A_{22}}{2} \left[\frac{\partial v_0}{\partial y} + \left(\frac{\partial w_0}{\partial y} \right)^2 \right] \right\} \frac{\partial H_3}{\partial y} dx dy \\
&+ \iint A_{66} \frac{\partial H_3^T}{\partial x} \left(\frac{1}{2} \frac{\partial u_0}{\partial y} + \frac{1}{2} \frac{\partial v_0}{\partial x} + \frac{\partial w_0}{\partial x} \frac{\partial w_0}{\partial y} \right) \frac{\partial H_3}{\partial y} dx dy \\
&+ \iint A_{66} \frac{\partial H_3^T}{\partial y} \left(\frac{1}{2} \frac{\partial u_0}{\partial y} + \frac{1}{2} \frac{\partial v_0}{\partial x} + \frac{\partial w_0}{\partial x} \frac{\partial w_0}{\partial y} \right) \frac{\partial H_3}{\partial x} dx dy \\
&+ \iint SA_{55} \frac{\partial H_3^T}{\partial x} \frac{\partial H_3}{\partial x} dx dy + \iint SA_{44} \frac{\partial H_3^T}{\partial y} \frac{\partial H_3}{\partial y} dx dy \\
{}^e k_{34} &= \iint SA_{55} \frac{\partial H_3^T}{\partial x} H_4 dx dy \\
{}^e k_{35} &= \iint SA_{44} \frac{\partial H_3^T}{\partial y} H_5 dx dy \\
{}^e k_{41} &= 0 \\
{}^e k_{42} &= 0 \\
{}^e k_{43} &= \iint SA_{55} H_4^T \frac{\partial H_3}{\partial x} dx dy \\
{}^e k_{44} &= \iint D_{11} \frac{\partial H_4^T}{\partial x} \frac{\partial H_4}{\partial x} dx dy + \iint D_{66} \frac{\partial H_4^T}{\partial y} \frac{\partial H_4}{\partial y} dx dy \\
&+ \iint SA_{55} H_4^T H_4 dx dy \\
{}^e k_{45} &= \iint D_{12} \frac{\partial H_4^T}{\partial x} \frac{\partial H_5}{\partial y} dx dy + \iint D_{66} \frac{\partial H_4^T}{\partial y} \frac{\partial H_5}{\partial x} dx dy \\
{}^e k_{51} &= 0 \\
{}^e k_{52} &= 0 \\
{}^e k_{53} &= \iint SA_{44} H_5^T \frac{\partial H_3}{\partial y} dx dy \\
{}^e k_{54} &= \iint D_{12} \frac{\partial H_5^T}{\partial y} \frac{\partial H_4}{\partial x} dx dy + \iint D_{66} \frac{\partial H_5^T}{\partial x} \frac{\partial H_4}{\partial y} dx dy \\
{}^e k_{55} &= \iint D_{22} \frac{\partial H_5^T}{\partial y} \frac{\partial H_5}{\partial y} dx dy + \iint D_{66} \frac{\partial H_5^T}{\partial x} \frac{\partial H_5}{\partial x} dx dy \\
&+ \iint SA_{44} H_5^T H_5 dx dy
\end{aligned}$$

References

- [1] Liu, C., Liu, J., Zhang, Y., Jin, S., Wang, C., and Lai, X., 2019, "Study on the Propagation of Dimensional Deviation in the Hull Block Building Process," *J. Ship Prod. Des.*
- [2] Jiao, Z., and Xing, Y., 2018, "Clamping-Sequence Optimisation Based on Heuristic Algorithm for Sheet-Metal Components," *Int. J. Prod. Res.*, **56**(24), pp. 7190–7200.
- [3] Wang, J., Rashed, S., and Murakawa, H., 2014, "Mechanism Investigation of Welding Induced Buckling Using Inherent Deformation Method," *Thin-Walled Struct.*, **80**, pp. 103–119.
- [4] Wang, R., Zhang, J., Serizawa, H., and Murakawa, H., 2009, "Study of Welding Inherent Deformations in Thin Plates Based on Finite Element Analysis Using Interactive Substructure Method," *Mater. Des.*, **30**(9), pp. 3474–3481.
- [5] Liu, S. C., and Hu, S. J., 1997, "Variation Simulation for Deformable Sheet Metal Assemblies Using Finite Element Methods," *ASME J. Manuf. Sci. Eng.*, **119**(3), pp. 368–374.
- [6] Jin, J., and Shi, J., 1999, "State Space Modeling of Sheet Metal Assembly for Dimensional Control," *ASME J. Manuf. Sci. Eng.*, **121**(4), pp. 756–762.
- [7] Liang, W., Deng, D., Sone, S., and Murakawa, H., 2005, "Prediction of Welding Distortion by Elastic Finite Element Analysis Using Inherent Deformation Estimated Through Inverse Analysis," *Welding The World*, **49**(11–12), pp. 30–39.
- [8] Lindgren, L., 2001, "Finite Element Modeling and Simulation of Welding. Part 3: Efficiency and Integration," *J. Therm. Stresses*, **24**(4), pp. 305–334.
- [9] Murakawa, H., Deng, D., Rashed, S., and Sato, S., 2009, "Prediction of Distortion Produced on Welded Structures During Assembly Using Inherent Deformation and Interface Element," *Trans. JWRI*, **38**(2), pp. 63–69.
- [10] Murakawa, H., Ma, N., and Huang, H., 2015, "Iterative Substructure Method Employing Concept of Inherent Strain for Large-Scale Welding Problems," *Welding World*, **59**(1), pp. 53–63.
- [11] Huang, H., Wang, J., Li, L., and Ma, N., 2016, "Prediction of Laser Welding Induced Deformation in Thin Sheets by Efficient Numerical Modeling," *J. Mater. Process. Technol.*, **227**, pp. 117–128.
- [12] Cai, W. W., Hsieh, C.-C., Long, Y., Marin, S. P., and Oh, K. P., 2006, "Digital Panel Assembly Methodologies and Applications for Compliant Sheet Components," *ASME J. Manuf. Sci. Eng.*, **128**(1), pp. 270–279.
- [13] Mazur, M., Leary, M., and Subic, A., 2011, "Computer Aided Tolerancing (CAT) Platform for the Design of Assemblies Under External and Internal Forces," *Computer-Aided Des.*, **43**(6), pp. 707–719.
- [14] Lee, B., Shalaby, M. M., Collins, R. J., Crisan, V., Walls, S. A., Robinson, D. M., and Saitou, K., "Variation Analysis of Three Dimensional Non-Rigid Assemblies," Proceedings of 2007 IEEE International Symposium on Assembly and Manufacturing, Ann Arbor, MI, July 22–25, IEEE, pp. 13–18.
- [15] Pahkamaa, A., Wärmefjord, K., Karlsson, L., Söderberg, R., and Goldak, J., 2012, "Combining Variation Simulation With Welding Simulation for Prediction of Deformation and Variation of a Final Assembly," *ASME J. Comput. Inf. Sci. Eng.*, **12**(2), p. 021002.
- [16] Wang, J., Han, J., Domblesky, J. P., Li, Z., Zhao, Y., and Sun, L., 2017, "A Plane Stress Model to Predict Angular Distortion in Single Pass Butt Welded Plates With Weld Reinforcement," *ASME J. Manuf. Sci. Eng.*, **139**(5), p. 051012.
- [17] Lorin, S. C., Cromvik, C., Edelvik, F., Lindkvist, L., and Söderberg, R., 2014, "Variation Simulation of Welded Assemblies Using a Thermo-Elastic Finite Element Model," *ASME J. Comput. Inf. Sci. Eng.*, **14**(3), p. 031003.
- [18] Yu, K., Jin, S., Lai, X., and Xing, Y., 2008, "Modeling and Analysis of Compliant Sheet Metal Assembly Variation," *Assem. Autom.*, **28**(3), pp. 225–234.
- [19] Dahlström, S., and Lindkvist, L., 2007, "Variation Simulation of Sheet Metal Assemblies Using the Method of Influence Coefficients With Contact Modeling," *ASME J. Manuf. Sci. Eng.*, **129**(3), pp. 615–622.
- [20] Lupuleac, S., Kovtun, M., Rodionova, O., and Marguet, B., 2009, "Assembly Simulation of Riveting Process," *SAE Int. J. Aerosp.*, **2**(1), pp. 193–198.
- [21] Camelio, J., Hu, S. J., and Ceglarek, D., 2003, "Modeling Variation Propagation of Multi-Station Assembly Systems With Compliant Parts," *ASME J. Mech. Des.*, **125**(4), pp. 673–681.
- [22] Yue, J., Camelio, J. A., Chin, M., and Cai, W., 2007, "Product-Oriented Sensitivity Analysis for Multistation Compliant Assemblies," *ASME J. Mech. Des.*, **129**(8), pp. 844–851.
- [23] Zhang, T., and Shi, J., 2016, "Stream of Variation Modeling and Analysis for Compliant Composite Part Assembly—Part I: Single-Station Processes," *ASME J. Manuf. Sci. Eng.*, **138**(12), p. 121003.
- [24] Zhang, T., and Shi, J., 2016, "Stream of Variation Modeling and Analysis for Compliant Composite Part Assembly—Part II: Multistation Processes," *ASME J. Manuf. Sci. Eng.*, **138**(12), p. 121004.
- [25] Söderberg, R., Wärmefjord, K., and Lindkvist, L., 2015, "Variation Simulation of Stress During Assembly of Composite Parts," *CIRP Ann. Manuf. Technol.*, **64**(1), pp. 17–20.
- [26] Xing, Y., 2017, "Fixture Layout Design of Sheet Metal Parts Based on Global Optimization Algorithms," *ASME J. Manuf. Sci. Eng.*, **139**(10), p. 101004.
- [27] Lorin, S., Lindkvist, L., and Söderberg, R., 2014, "Variation Simulation of Stresses Using the Method of Influence Coefficients," *ASME J. Comput. Inf. Sci. Eng.*, **14**(1), p. 011001.
- [28] Jin, S., Yu, K., Lai, X., and Liu, Y., 2009, "Sensor Placement Strategy for Fixture Variation Diagnosis of Compliant Sheet Metal Assembly Process," *Assembly Autom.*, **29**(4), pp. 358–363.
- [29] Lupuleac, S., Zaitseva, N., Stefanova, M., Berezin, S., Shinder, J., Petukhova, M., and Bonhomme, E., 2019, "Simulation of the Wing-to-Fuselage Assembly Process," *ASME J. Manuf. Sci. Eng.*, **141**(6), p. 061009.
- [30] Lupuleac, S., Zaitseva, N., Petukhova, M., Shinder, J., Berezin, S., Khashba, V., and Bonhomme, E., 2017, "Combination of Experimental and Computational Approaches to A320 Wing Assembly," No. 0148-7191, SAE Technical Paper.
- [31] Petukhova, M. V., Lupuleac, S. V., Shinder, Y. K., Smirnov, A. B., Yakunin, S. A., and Bretagnol, B., 2014, "Numerical Approach for Airframe Assembly Simulation," *J. Math. Ind.*, **4**(1), p. 8.
- [32] Choi, W., and Chung, H., 2015, "Variation Simulation of Compliant Metal Plate Assemblies Considering Welding Distortion," *ASME J. Manuf. Sci. Eng.*, **137**(3), p. 031008.
- [33] Choi, W., and Chung, H., 2018, "Variation Simulation Model for pre-Stress Effect on Welding Distortion in Multi-Stage Assemblies," *Thin-Walled Struct.*, **127**, pp. 832–843.
- [34] Liu, T., Li, Z.-M., Jin, S., and Chen, W., 2019, "Compliant Assembly Analysis Including Initial Deviations and Geometric Nonlinearity—Part I: Beam

- Structure,” Proceedings of the Institution of Mechanical Engineers, Part C: Journal of Mechanical Engineering Science, 233(12), pp. 4233–4246.
- [35] Liu, T., Li, Z.-M., Jin, S., and Chen, W., 2019, “Compliant Assembly Analysis Including Initial Deviations and Geometric Nonlinearity, Part II: Plate Structure,” *Proc. Inst. Mech. Eng. Part C: J. Mech. Eng. Sci.*, **233**(11), pp. 3717–3732.
- [36] Liu, T., Li, Y., Li, B., Li, Z., Yao, L., and Jin, S., “Compliant Variation Analysis for High-Speed Train With Consideration of Welding Distortion,” Proceedings of ASME 2018 International Mechanical Engineering Congress and Exposition, American Society of Mechanical Engineers, David L. Lawrence Convention Center, PA, Nov. 9–14, American Society of Mechanical Engineers, p. V002T002A107.
- [37] Stewart, M. L., and Chase, K. W., 2004, “Variation Simulation of Fixtured Assembly Processes for Compliant Structures Using Piecewise-Linear Analysis,” Proceedings of ASME 2005 International Mechanical Engineering Congress and Exposition, Nov. 5–11, 2005, Orlando, FL, Paper No: IMECE2005-82371, pp. 591–600.
- [38] Reddy, J. N., 2006, *Theory and Analysis of Elastic Plates and Shells*, CRC Press, Boca Raton, FL.
- [39] Sun, W., and Yuan, Y.-X., 2006, *Optimization Theory and Methods: Nonlinear Programming*, Springer Science & Business Media, Berlin, Germany.
- [40] Ba, S., and Joseph, V. R., 2012, “Composite Gaussian Process Models for Emulating Expensive Functions,” *Annals Appl. Stat.*, **6**(4), pp. 1838–1860.
- [41] Ba, S., and Joseph, V. R., 2018, “Composite Gaussian Process Models. R package version 2.1-1,” <https://CRAN.R-project.org/package=CGP>, Accessed 1 May 2019.
- [42] Sulaiman, M. S., Manurung, Y. H. P., Graf, M., and Bauer, A., 2018, “Analysis of Weld Induced Distortion of Butt Joint Using Simulation and Experimental Study,” *J. Mech. Eng.*, **5**(2), pp. 78–89.
- [43] Goldak, J. A., and Akhlaghi, M., 2006, *Computational Welding Mechanics*, Springer Science & Business Media, Berlin, Germany.
- [44] Islam, M. R., Buijk, A., Raisrohani, M., and Motoyama, K., 2015, “Process Parameter Optimization of Lap Joint Fillet Weld Based on FEM-RSM-GA Integration Technique,” *Adv. Eng. Software*, **79**, pp. 127–136.